

Transformer based Pluralistic Image Completion with Reduced Information Loss

Qiankun Liu, Yuqi Jiang, Zhentao Tan, Dongdong Chen[†], Ying Fu[†], *Senior Member, IEEE*, Qi Chu[†], Gang Hua, *Fellow, IEEE*, Nenghai Yu

Abstract—Transformer based methods have achieved great success in image inpainting recently. However, we find that these solutions regard each pixel as a token, thus suffering from an information loss issue from two aspects: 1) They downsample the input image into much lower resolutions for efficiency consideration. 2) They quantize 256^3 RGB values to a small number (such as 512) of quantized color values. The indices of quantized pixels are used as tokens for the inputs and prediction targets of the transformer. To mitigate these issues, we propose a new transformer based framework called “PUT”. Specifically, to avoid input downsampling while maintaining computation efficiency, we design a patch-based auto-encoder P-VQVAE. The encoder converts the masked image into non-overlapped patch tokens and the decoder recovers the masked regions from the inpainted tokens while keeping the unmasked regions unchanged. To eliminate the information loss caused by input quantization, an Un-quantized Transformer is applied. It directly takes features from the P-VQVAE encoder as input without any quantization and only regards the quantized tokens as prediction targets. Furthermore, to make the inpainting process more controllable, we introduce semantic and structural conditions as extra guidance. Extensive experiments show that our method greatly outperforms existing transformer based methods on image fidelity and achieves much higher diversity and better fidelity than state-of-the-art pluralistic inpainting methods on complex large-scale datasets (e.g., ImageNet). Codes are available at <https://github.com/liuqk3/PUT>.

Index Terms—Image Completion, Image Inpainting, Image Reconstruction, Transformers, Vector Quantization, Diversity, Fidelity

1 INTRODUCTION

IMAGE inpainting, which focuses on filling meaningful and plausible contents in missing regions for damaged images, is a hot topic in the computer vision field and widely used in various real applications [1], [2], [3], [4], [5]. Traditional methods [3], [6], [7] based on texture matching can handle simple cases very well but struggle for complex natural images. In the last several years, benefiting from the development of CNNs, tremendous success [8], [9] has been achieved by learning on large-scale datasets. However, due to the inherent properties of CNNs, *i.e.*, local inductive bias and spatial-invariant kernels, such methods still do not perform well in understanding global structure and inpainting large masked/missing regions.

Recently, transformers have demonstrated their power in various vision tasks [12], [13], [14], [15], [16], thanks to their capability of modeling long-term relationships. Some recent works [10], [11] also attempt to apply transformers for image inpainting and have achieved remarkable success in better fidelity and large region inpainting quality. In addition, pluralistic images can be produced when the content of masked regions is predicted and sampled in an autoregressive manner. As shown in the top row of Fig. 1, they follow a similar design: 1) Downsample the input

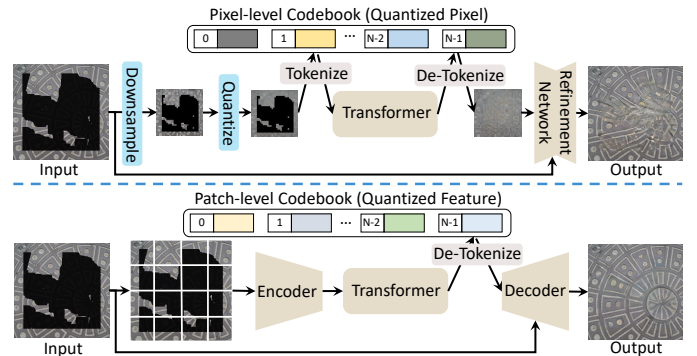


Fig. 1: Top: Existing transformer based autoregressive methods [10], [11]. The output is produced by ICT [10]. Bottom: Our transformer based method. “Tokenize” means getting the indices of quantized pixels or latent vectors, and “De-Tokenize” is the inverse operation.

image into lower resolutions and quantize the pixels. 2) Use the transformer to recover masked pixels by regarding each quantized pixel as the token. 3) Upsample and refine the low-resolution result by feeding it together with the original input image into an extra CNN network.

In this paper, we argue that using the above pixel-based token makes existing transformer based autoregressive solutions suffer from the information loss issue from two aspects: 1) *Downsampling*. To avoid the high computation complexity of the transformer, the input image is downsampled into a much lower resolution to reduce the input token number. 2) *Quantization*. To constrain the prediction within a small space, the huge amount (256^3 , in detail) of RGB pixel

- Qiankun Liu, Yuqi Jiang and Ying Fu are with the School of Computer Science and Technology, Beijing Institute of Technology (liuqk3@bit.edu.cn, yqjiang@bit.edu.cn).
- Zhentao Tan, Qi Chu and Nenghai Yu are with the School of Information Science and Technology, University of Science and Technology of China (tzf@mail.ustc.edu.cn; qchu, ynh@ustc.edu.cn).
- Dongdong Chen is with Microsoft Cloud AI (cdlyf@gmail.com).
- Gang Hua is with Wormpex AI Research LLC (ganghua@gmail.com).
- Dongdong Chen, Ying Fu and Qi Chu are co-corresponding authors.

values are quantized into much fewer (e.g., 512) quantized pixel values through clustering. The indices of quantized pixels are used as discrete tokens both for the input and prediction target of the transformer. Using the quantized input inevitably further results in information loss.

To mitigate the aforementioned issues, we propose a new transformer based autoregressive framework “PUT”, which is designed to reduce the information loss in existing inpainting transformers as much as possible. As shown in the bottom row of Fig. 1, the original high-resolution input image is directly fed into a *patch-based encoder without any downsampling*, and the transformer directly takes the features from the encoder as *input without any quantization*.

Specifically, PUT contains two key designs: Patch-based Vector Quantized Variational Auto-Encoder (“P-VQVAE”) and Un-Quantized Transformer (“UQ-Transformer”). P-VQVAE is a dedicatedly designed auto-encoder: 1) Its encoder converts each image patch into a feature vector in a non-overlapped way, where the non-overlapped design is to avoid the disturbance between masked and unmasked regions. 2) As the prediction space of UQ-Transformer, a dual-codebook is built for feature tokenization, where masked and unmasked patches are separately represented by different codebooks. 3) The decoder in P-VQVAE not only recovers the masked image regions from the inpainted tokens but also maintains unmasked regions unchanged. For UQ-Transformer, it utilizes the quantized tokens as the prediction targets for masked patches but takes the unquantized features from the encoder as input. Compared to taking the quantized discrete tokens as input, this design avoids information loss. Furthermore, to make the prediction process controllable, we allow end-users to provide semantic and structural conditions as extra guidance. Extensive experiments are conducted on FFHQ [17], Places2 [18], and ImageNet [19] to demonstrate the superiority of the proposed method. Benefiting from less information loss, PUT achieves much higher fidelity than existing transformer based autoregressive solutions and outperforms state-of-the-art pluralistic inpainting methods by a large margin in terms of diversity.

This work builds upon our previous CVPR paper. Compared with the conference paper, the main contributions in this paper include:

- We introduce a simple but effective mask embedding for UQ-Transformer to reduce the inpainted artifacts produced by the conference version method.
- We design a multi-token sampling strategy, which enables PUT to take 20× less inference time than the vanilla per-token sampling strategy.
- We propose to integrate the semantic and structural conditions into the generation process, making the final inpainting results more user-controllable.

In addition, more analysis experiments are conducted, including learning more latent vectors with Gumbel-softmax relaxation strategy, applying PUT to higher resolution images (512×512), controllable image inpainting with extra user guidance, comparing the number of FLOPs, parameters and inference time of different methods, analyzing the impact of the sampling strategy and mask embedding

on the quality of inpainted images, and applying pretrained PUT to downstream tasks.

2 RELATED WORK

2.1 Auto-Encoders

Auto-encoders [20] are a kind of network in unsupervised and semi-supervised learning, which can be divided into three categories: contractive auto-encoder (CAE) [21], regularized auto-encoder (RAE) [22], and variational auto-encoder (VAE) [23]. Among them, VAE is the generation model and has become one of the popular frameworks for image synthesis. With the designed two mapping modules between real data and latent space, called encoder and decoder, VAE can be trained in a self-supervised strategy. Diverse images can be generated through the decoder in VAE with latent space sampling or autoregressive models [24], [25]. Later, vector quantized variational auto-encoder (VQ-VAE) [26], [27] is proposed for discrete representation learning to circumvent issues of “posterior collapse”, and further developed by VQ-VAE-2 [28]. Recently, based on the similar quantization mechanism with VQ-VAE, VAGAN [15] and dVAE [16] are proposed for conditional image generation through transformers [29]. Different from previous methods, the proposed P-VQVAE is dedicated to image inpainting to avoid the disturbance between masked and unmasked regions but with the capability of image reconstruction.

2.2 Vision Transformers

Thanks to the capability of modeling long-range relationships, transformers have been widely used in different vision tasks, such as image recognition [13], [30], image synthesis [14], [15], [16], action recognition [31], image inpainting [10], [11], and multi-modality learning [32], [33]. Specifically, the autoregressive inference mechanism is naturally suitable for image synthesis related tasks, which can bring diverse results while guaranteeing the quality of the synthesized images [10], [14], [15], [16]. However, these methods use discrete tokens as the input of transformers. Such practice has a limited effect on image synthesis task but has a non-negligible impact on image inpainting task. In this paper, we propose to replace discrete tokens with continuous feature vectors to avoid information loss.

Recently, Masked Image Modeling (MIM) methods [30], [34], [35], [36], [37] are proposed for the pretraining of vision transformers with a similar pretext task of image inpainting. However, these methods aim at learning useful representations from incomplete images, leaving the visual quality unpleasant. Different from MIM models, PUT focuses on generating high-quality diverse images with the arbitrary shapes of masks. Nonetheless, the pretrained transformer in PUT learns useful priors for downstream tasks.

2.3 Image Inpainting

According to the diversity of inpainted images, there are two different types of definitions for image inpainting task: deterministic image inpainting and pluralistic image inpainting. Most of the traditional methods, whether diffusion-based methods [38], [39] or patch-based methods [3], [40], can only generate a single result for each

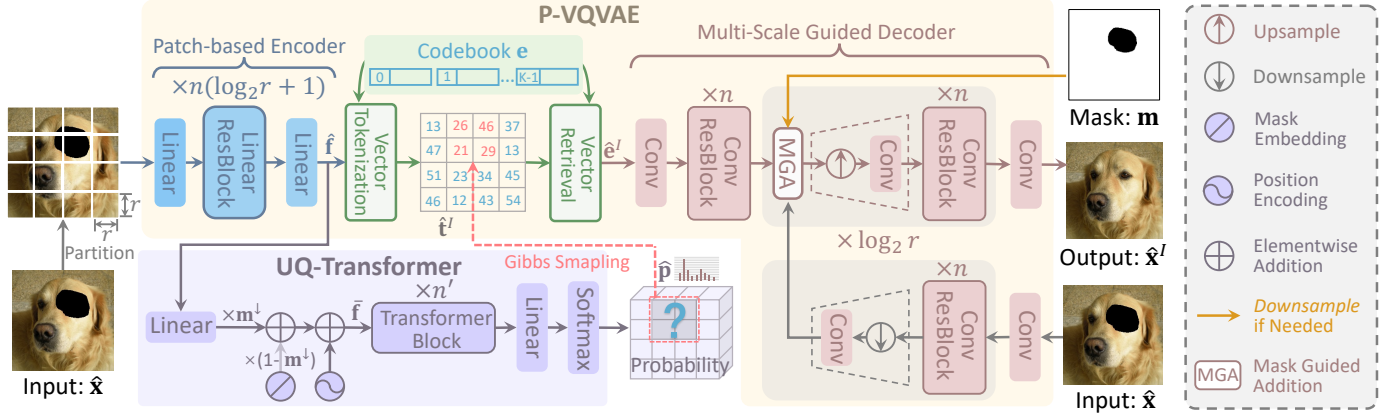


Fig. 2: Pipeline of PUT for pluralistic image inpainting without condition. The input image is divided into non-overlapped patches which are processed by the encoder independently. The unmasked regions are reconstructed by the decoder, while the masked regions are predicted by the transformer.

input and may fail while meeting large areas of missing pixels. Later, some CNN based methods [8], [9], [41], [42] are proposed to ensure consistency of the semantic content of the inpainted images but still ignore the diversity of results. PICNet [43] and UCTGAN [44] generate diverse results from the modeled distribution for the masked images. Recently, CoModGAN [45] and MAT [46] follow the model structure of StyleGAN2 [47] to get diverse results with sampled noise and achieve impressive fidelity on monotonous datasets, *e.g.*, FFHQ [17] for faces. However, the diversity of these two methods is very limited and they fail to get reasonable results on complex datasets like ImageNet [19]. Different from the above-mentioned methods, transformer based solutions [10], [11] produce diverse results by sampling the tokens of masked patches iteratively in an autoregressive manner. However, their unreasonable design, like the downsampling of input images and quantization of transformer inputs, results in a serious information loss issue. Thus, we propose a novel framework to maximize the input information to achieve better inpainted results. Furthermore, we introduce two types of conditions to make the inpainted results controllable for users.

3 METHOD

Our PUT mainly consists of a Patch-based Vector Quantized Variational Auto-Encoder (P-VQVAE) and an Un-Quantized transformer (UQ-Transformer). The overview of our method is shown in Fig. 2. Let $\mathbf{x} \in \mathbb{R}^{H \times W \times 3}$ be an image and $\mathbf{m} \in \{0, 1\}^{H \times W \times 1}$ be the mask denoting whether a pixel needs to be inpainted (with value 0) or not (with value 1). H and W are the spatial resolution. The image $\hat{\mathbf{x}} = \mathbf{x} \otimes \mathbf{m}$ is the masked image that contains missing pixels, where \otimes is the element-wise multiplication. The masked image $\hat{\mathbf{x}}$ is first fed into the encoder of P-VQVAE to get the patch-based feature vectors. Then UQ-Transformer takes the feature vectors as input and predicts the tokens (*i.e.*, indices) of latent vectors in a codebook for masked regions. Finally, the retrieved latent vectors are fed into the decoder of P-VQVAE to reconstruct the inpainted image, which is guided by the input image from a reference branch.

3.1 P-VQVAE

P-VQVAE contains a patch-based encoder that maps image patches to feature vectors, a dual-codebook that quantizes feature vectors to discrete tokens, and a multi-scale guided decoder that recovers inpainted images from tokens by referring to the input masked images.

3.1.1 Patch-based Encoder

Conventional CNN based encoders process the input image with several convolution kernels in a sliding window manner, which is unsuitable for image inpainting for transformers since the disturbance between masked and unmasked regions is introduced. Thus, the encoder of P-VQVAE (denoted as P-Enc) is designed to process the input image by several linear layers in a non-overlapped patch manner. Specifically, the masked image $\hat{\mathbf{x}}$ is first partitioned into $\frac{H}{r} \times \frac{W}{r}$ non-overlapped patches, where r is the spatial size of patches. For a patch, we call it a *masked patch* if it contains any missing pixels, otherwise an *unmasked patch*. Each patch is flattened and then mapped into a feature vector. Formally, all feature vectors are denoted as $\hat{\mathbf{f}} = \mathcal{E}(\hat{\mathbf{x}}) \in \mathbb{R}^{\frac{H}{r} \times \frac{W}{r} \times D}$, where D (set to 256 by default) is the dimension of feature vectors and $\mathcal{E}(\cdot)$ is the encoder function.

3.1.2 Dual-Codebook for Vector Quantization

Following previous works [15], [26], [28], the feature vectors from the encoder are quantized into discrete tokens with the latent vectors in the learnable codebook. But differently, we design a dual-codebook (denoted as D-Codes) for vector quantization, which is more suitable for image inpainting. In D-Codes, the latent vectors are divided into two types, denoted as $\mathbf{e} \in \mathbb{R}^{K \times D}$ and $\mathbf{e}' \in \mathbb{R}^{K' \times D}$, which are responsible for feature vectors that are mapped from unmasked and masked patches, respectively. K and K' are the number of latent vectors. Let $\mathbf{m}^\downarrow \in [0, 1]^{\frac{H}{r} \times \frac{W}{r} \times 1}$ be the unmasked ratio of image patches, *i.e.*, the ratio of the number of unmasked pixels to r^2 . It is used as an indicator mask that indicates whether a patch is a masked (with a value less than 1) or unmasked (with a value equal to 1) patch. For each feature vector $\hat{\mathbf{f}}_{i,j}$ in $\hat{\mathbf{f}}$, we use $\mathbf{d}_{i,j} \in \mathbb{R}^K$ and $\mathbf{d}'_{i,j} \in \mathbb{R}^{K'}$ as the

Euclidean distance between $\hat{\mathbf{f}}_{i,j}$ and the latent vectors in \mathbf{e} and \mathbf{e}' . The quantized vector for $\hat{\mathbf{f}}_{i,j}$ is obtained as:

$$\begin{cases} \mathbf{e}_k \text{ where } k = \min_{\text{ind}}[\mathbf{d}_{i,j}], \text{ if } \mathbf{m}_{i,j}^\downarrow = 1, \\ \mathbf{e}'_{k'} \text{ where } k' = \min_{\text{ind}}[\mathbf{d}'_{i,j}], \text{ else,} \end{cases} \quad (1)$$

where $\min_{\text{ind}}[\cdot]$ is the operation that gets the index of the minimum element in the given vector. The quantized vectors and tokens for $\hat{\mathbf{f}}$ are denoted as $\hat{\mathbf{e}} \in \mathbb{R}^{\frac{H}{r} \times \frac{W}{r} \times D}$ and $\hat{\mathbf{t}} = \mathcal{I}(\hat{\mathbf{f}}, \mathbf{e}, \mathbf{e}', \mathbf{m}^\downarrow) \in \mathbb{N}^{\frac{H}{r} \times \frac{W}{r}}$, where $\mathcal{I}(\cdot, \cdot, \cdot, \cdot)$ is the function that gets tokens for its first argument by getting the indices of all quantized vectors in $\hat{\mathbf{e}}$.

3.1.3 Multi-Scale Guided Decoder

For the image inpainting task, an indisputable fact is that the unmasked regions should be kept unchanged. To this end, we design a multi-scale guided decoder, denoted as MSG-Dec, to construct the inpainted image $\hat{\mathbf{x}}^I$ by referencing the input masked image $\hat{\mathbf{x}}$. Let $\hat{\mathbf{t}}^I$ be the inpainted tokens by transformer (Ref. Section 3.3) and $\hat{\mathbf{e}}^I$ be the retrieved quantized vectors from the codebook based on $\hat{\mathbf{t}}^I$. The construction procedure is formulated as:

$$\hat{\mathbf{x}}^I = \mathcal{D}(\hat{\mathbf{e}}^I, \mathbf{m}, \hat{\mathbf{x}}), \quad (2)$$

where $\mathcal{D}(\cdot, \cdot, \cdot)$ is the decoder function. The decoder consists of two branches: 1) a main branch which starts with the quantized vectors $\hat{\mathbf{e}}^I$ and uses several upsampling operations and convolution layers to generate inpainted images. 2) a reference branch that extracts multi-scale feature maps (with spatial sizes $\frac{H}{2^l} \times \frac{W}{2^l}$, $0 \leq l \leq \log_2 r$) from the input masked image $\hat{\mathbf{x}}$. The features from the reference branch are fused to the features with the same scale from the main branch through a Mask Guided Addition (MGA) module that is defined below:

$$\hat{\mathbf{e}}^{I,l-1} = \mathcal{D}_{l-1}((1 - \text{int}[\mathbf{m}^{\downarrow,l}]) \otimes \hat{\mathbf{e}}^{I,l} \oplus \text{int}[\mathbf{m}^{\downarrow,l}] \otimes \hat{\mathbf{f}}^{R,l}), \quad (3)$$

where $\hat{\mathbf{e}}^{I,l}$ and $\hat{\mathbf{f}}^{R,l}$ are the features with spatial size $\frac{H}{2^l} \times \frac{W}{2^l}$ from the main branch and the reference branch, respectively. $\mathbf{m}^{\downarrow,l}$ is the unmasked ratio obtained from \mathbf{m} for the corresponding spatial size. \oplus is the elementwise addition operation. $\mathcal{D}_{l-1}(\cdot)$ is the sub-network in the main branch that consists of an upsampling operation, a convolution layer, and several Conv ResBlocks. By removing the reference branch in the decoder, P-VQVAE is also capable of reconstructing the input image $\hat{\mathbf{x}}$ like other auto-encoders.

3.1.4 Training of P-VQVAE

The decoder of P-VQVAE learns to reconstruct the inpainted image based on not only the retrieved quantized vectors but also the input masked image from the reference branch. Therefore, to avoid the decoder learning to reconstruct the input image $\hat{\mathbf{x}}$ only from the reference image, we get the reference image by randomly erasing some pixels in $\hat{\mathbf{x}}$ with another mask \mathbf{m}' (see in Fig. 3). Let $\hat{\mathbf{x}}^R = \mathcal{D}(\hat{\mathbf{e}}, \mathbf{m} \otimes \mathbf{m}', \hat{\mathbf{x}} \otimes \mathbf{m}')$ be the reconstructed image. In our design, the unmasked pixels in the reference image are utilized to recover the corresponding pixels in $\hat{\mathbf{x}}^R$, while the latent vectors in codebook \mathbf{e}' and \mathbf{e} are used to recover the pixels in $\hat{\mathbf{x}}^R$ masked by \mathbf{m} and the remaining pixels, respectively. P-VQVAE is trained with the commonly used VQ-VAE loss [26]. Please refer to our conference paper [48] for more details.

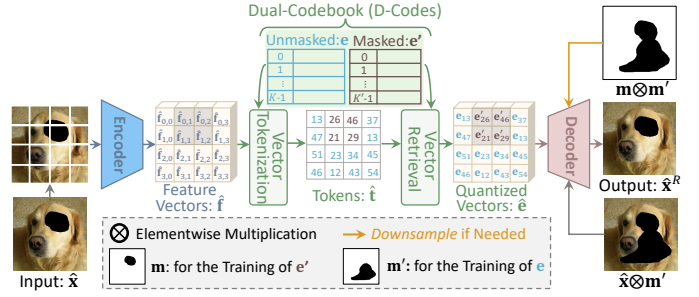


Fig. 3: Training procedure of P-VQVAE. The unmasked pixels in the reference image $\hat{\mathbf{x}} \otimes \mathbf{m}'$ are utilized to recover the corresponding pixels in $\hat{\mathbf{x}}^R$, while the latent vectors in codebook \mathbf{e}' and \mathbf{e} are used to recover the pixels in $\hat{\mathbf{x}}^R$ masked by \mathbf{m} and the remaining pixels, respectively.

3.1.5 Learning More Latent Vectors

Different from the settings in our conference paper, more latent vectors in the codebook are learned in this work to help the model distinguish more patterns and textures. However, when the number of latent vectors in codebook \mathbf{e} is increased, for example, from 512 to 8192, we empirically find that only a few of them are used (about 3000). To handle this, we learn the latent vectors with Gumbel-Softmax relaxation [49] in the training stage. The core idea in Gumbel-Softmax relaxation is to add some noise to the distance between feature vectors and latent vectors, so as to avoid the phenomenon that only a subset of latent vectors are used. Specifically, the quantized vector for feature vector $\hat{\mathbf{f}}_{i,j}$ obtained in Eq. (1) is rewritten as:

$$\begin{cases} \mathbf{e}_k \text{ where } k = \min_{\text{ind}}[-\mathcal{S}(\mathbf{n} \ominus \mathbf{d}_{i,j}, \tau)], \text{ if } \mathbf{m}_{i,j}^\downarrow = 1 \\ \mathbf{e}'_{k'} \text{ where } k' = \min_{\text{ind}}[-\mathcal{S}(\mathbf{n}' \ominus \mathbf{d}'_{i,j}, \tau)], \text{ else,} \end{cases} \quad (4)$$

where $\mathbf{n} \in \mathbb{R}^K$ and $\mathbf{n}' \in \mathbb{R}^{K'}$ are the sampled Gumbel noises, $\mathcal{S}(\cdot, \tau)$ is the softmax function applied to its first argument with temperature τ . More training details are provided in Section 4.2.

3.2 UQ-Transformer

In existing transformers for image inpainting [10] and synthesis [15], [16], the quantized discrete tokens are used as both the inputs and prediction targets. Given such discrete tokens, transformers suffer from the severe input information loss issue, which is harmful to their prediction. In contrast, to take full advantage of feature vectors $\hat{\mathbf{f}}$ from the encoder of P-VQVAE, our UQ-Transformer takes $\hat{\mathbf{f}}$ rather than the discrete tokens as inputs and predicts the discrete tokens for masked patches.

3.2.1 Mask Embedding

As a common practice, a set of position embeddings $\mathbf{f}^P \in \mathbb{R}^{\frac{H}{r} \times \frac{W}{r} \times D'}$ is learned to introduce positional induction in transformers, where D' is the hidden dimensionality before UQ-Transformer. However, we find that UQ-Transformer cannot distinguish the patch embeddings for masked and unmasked patches effectively. The reasons come from two folds: 1) The numbers of missing pixels in different masked patches are not restricted to be the same. 2) The missing

pixels in a masked image are set to zeros, which are the same as unmasked *black* pixels. This makes PUT produce some artifacts with *black* pixels in masked regions easily when the image contains some natural black pixels, which will be analyzed in the following Section 4.7.2. To alleviate this issue, we introduce a simple yet effective mask embedding $\mathbf{f}^M \in \mathbb{R}^{1 \times 1 \times D'}$. Similar to the position embeddings \mathbf{f}^P , the mask embedding \mathbf{f}^M is also learned during the training stage. But differently, the image patches in different locations share the same mask embedding. Let $\bar{\mathbf{f}} \in \mathbb{R}^{\frac{H}{r} \times \frac{W}{r} \times D'}$ be the input features of the first transformer block, it can be obtained as:

$$\bar{\mathbf{f}} = (\mathbf{m}^\downarrow \otimes \mathcal{F}(\hat{\mathbf{f}}) \oplus (1 - \mathbf{m}^\downarrow) \otimes \mathbf{f}^M) \oplus \mathbf{f}^P, \quad (5)$$

where $\mathcal{F}(\cdot)$ is a linear layer that adjusts the dimensionality of the input features. The features of image patches are added with mask embedding according to their mask ratios \mathbf{m}^\downarrow , which helps the model distinguish the unmasked and masked patches, as well as the masked patches that with different numbers of missing pixels.

3.2.2 Prediction of UQ-Transformer

The output of the last transformer block is projected to the distribution over K latent vectors in codebook \mathbf{e} with a linear layer and a softmax function. We formulate the above procedure as $\hat{\mathbf{p}} = \mathcal{T}(\hat{\mathbf{f}}) \in [0, 1]^{\frac{H}{r} \times \frac{W}{r} \times K}$, where $\mathcal{T}(\cdot)$ refers to the UQ-Transformer function. With the predicted probability, the tokens for masked patches can be sampled.

The intuition behind this design is that UQ-Transformer learns the likelihood of the tokens for masked patches given the unmasked patch embeddings. Let $\Pi = \{(i, j) | \mathbf{m}_{i,j}^\downarrow < 1\}$ be the index set of masked patches. For each masked patch with index (i, j) , the likelihood can be denoted as $p(\hat{\mathbf{t}}_{i,j}^I | \hat{\mathbf{f}}_\Pi) = \hat{\mathbf{p}}_{i,j}$, where $\bar{\Pi}$ is the complementary set of Π , *i.e.*, the index set of unmasked patches.

3.2.3 Training of UQ-Transformer

Given a masked image $\hat{\mathbf{x}}$, the distribution of its corresponding inpainted tokens over K latent vectors can be obtained with the pre-trained P-VQVAE and UQ-Transformer $\hat{\mathbf{p}} = \mathcal{T}(\mathcal{E}(\hat{\mathbf{x}}))$. The ground-truth tokens for \mathbf{x} are $\mathbf{t} = \mathcal{I}(\mathcal{E}(\mathbf{x}), \mathbf{e}, \mathbf{e}', \mathcal{O}(\mathbf{m}^\downarrow))$ (Ref. Section 3.1.2), where $\mathcal{O}(\cdot)$ sets all values in the given argument to 1. UQ-Transformer is trained with a classification loss by fixing P-VQVAE:

$$L_{trans} = -\frac{1}{|\Pi|} \sum_{(i,j) \in \Pi} \log(\hat{\mathbf{p}}_{i,j, \mathbf{t}_{i,j}}). \quad (6)$$

In order to make the training stage consistent with the inference stage, where only the quantized vectors can be obtained for masked regions, we randomly quantize the feature vectors in $\mathcal{E}(\hat{\mathbf{x}})$ to the latent vectors in the codebook with probability 0.3 before feeding it to UQ-Transformer.

3.3 Sampling Strategy for Image Inpainting

In order to get diverse results, existing transformer based works usually adopt a per-token sampling strategy for image synthesis [15], [16], [50] and inpainting [10], *i.e.*, the tokens are sampled one-by-one. Formally, let $\bar{\Pi}^I$ be the index set of previously inpainted patches and $\hat{\mathbf{e}}_{\bar{\Pi}^I}^I$ be the

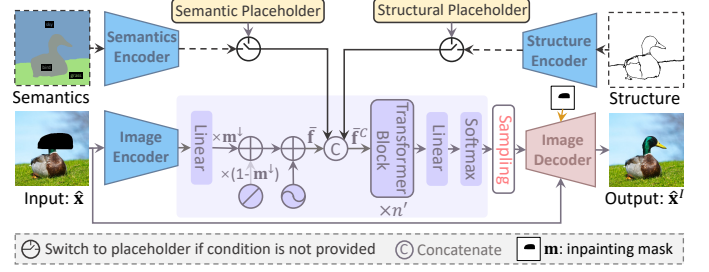


Fig. 4: The pipeline of controllable image inpainting. Users are free to provide none, one, or both of these two conditions.

retrieved latent vectors for inpainted patches. The likelihood of masked patch (i, j) is obtained given the unmasked patches embeddings $\hat{\mathbf{f}}_\Pi$ and the retrieved latent vectors $\hat{\mathbf{e}}_{\bar{\Pi}^I}^I$:

$$p(\hat{\mathbf{t}}_{i,j}^I | \hat{\mathbf{f}}_\Pi, \hat{\mathbf{e}}_{\bar{\Pi}^I}^I) = \mathcal{T}(\mathcal{R}(\hat{\mathbf{f}}, \hat{\mathbf{e}}_{\bar{\Pi}^I}^I))_{i,j}, \quad (7)$$

where $\mathcal{R}(\hat{\mathbf{f}}, \hat{\mathbf{e}}_{\bar{\Pi}^I}^I)$ replaces the feature vectors of masked patches in $\hat{\mathbf{f}}$ with retrieved latent vectors $\hat{\mathbf{e}}_{\bar{\Pi}^I}^I$ according to the indices in $\bar{\Pi}^I$. $|\Pi|$ iterations are required to finish the inpainting process, which is time-consuming.

To better balance the inference time and image quality, we design a multi-token sampling strategy. The overall multi-token sampling strategy is divided into two steps: 1) selecting the patches to be inpainted, and 2) sampling the tokens for selected patches. Specifically, in each iteration, we first get an index set, denoted as Π^I , of masked patches with top- \mathcal{K}_1 maximum predicted probabilities among the remaining masked patches:

$$\Pi^I = \text{TopK}_{\text{ind}}[\max[\mathcal{T}(\mathcal{R}(\hat{\mathbf{f}}, \hat{\mathbf{e}}_{\bar{\Pi}^I}^I))]_{\Pi - \bar{\Pi}^I}, \mathcal{K}_1], \quad (8)$$

where $\max[\cdot]$ returns the maximum values of its argument along the last dimensionality, $\Pi - \bar{\Pi}^I$ is the indices of remaining masked patches and $\text{TopK}_{\text{ind}}[\cdot, \mathcal{K}_1]$ gets the indices of the top- \mathcal{K}_1 maximum values in its first argument. Then the tokens for these \mathcal{K}_1 patches are simultaneously but independently sampled from the likelihood:

$$p(\hat{\mathbf{t}}_{\Pi^I}^I | \hat{\mathbf{f}}_\Pi, \hat{\mathbf{e}}_{\bar{\Pi}^I}^I) = \mathcal{T}(\mathcal{R}(\hat{\mathbf{f}}, \hat{\mathbf{e}}_{\bar{\Pi}^I}^I))_{\Pi^I}. \quad (9)$$

To avoid sampling the tokens that have low probabilities, we only maintain the top- \mathcal{K}_2 elements in the likelihood for each patch while sampling. The two parameters \mathcal{K}_1 and \mathcal{K}_2 mainly have impacts on inference speed and image quality, respectively. However, as we will see in Section 4.7.3, PUT is robust to different values of them to some extent. A special case of our multi-token sampling strategy is that $\mathcal{K}_1 = |\Pi|$, which means the tokens of all masked patches are simultaneously sampled in one iteration.

3.4 Controllable Image Inpainting

Though PUT generates photorealistic and diverse results for a masked image, it is hard for end-users to intervene in the sampling process to control the generated contents for masked regions. In this section, we introduce semantic and structural conditions (*i.e.*, segmentation and sketch maps) provided by users as extra guidance for PUT, making the inpainted results controllable, as shown in Fig. 4.

3.4.1 Semantic and Structural Maps as Features

Semantic and structural maps are intuitive to be drawn and understood by users. However, there are two challenges for the drawing of semantic maps: 1) the categories in real-world applications are open-set, while most existing high-quality segmentation models are trained on closed-set categories. 2) not all users are professional enough to categorize the content in an image and relate it to the supported categories accurately. To handle these challenges, we design a simple unknown category strategy that allows the user to label categories not included in the closed-set categories. Since an image may contain multiple unrecognized objects with different categories, multiple unknown categories are needed in the model. Therefore, we define a certain number of unknown categories. During the training procedure, we randomly select some of the known categories in the semantic map and use the same number of unknown categories to substitute them. During inference, if users encounter objects with categories not included in the closed-set categories, as shown in Fig. 12, the user can manually label these objects using multiple unknown categories.

Formally, we denote the user-provided semantic and structural maps with $\mathbf{c}_{sem} \in \{0, 1, \dots, C + U - 1\}^{H \times W \times 1}$ and $\mathbf{c}_{str} \in \{0, 1\}^{H \times W \times 1}$, where C is the number of known categories while U is the pre-defined number of unknown categories. Since the content of masked regions is predicted by UQ-Transformer in the feature domain, we need to map semantic and structural maps into feature representation as well. To this end, two P-VQVAEs (without reference branch) are trained to extract features from these two types of maps. The extracted features for semantic and structural maps are denoted as $\mathbf{f}_{sem}, \mathbf{f}_{str} \in \mathbb{R}^{\frac{H}{r} \times \frac{W}{r} \times D}$, respectively.

3.4.2 Semantic and Structural Features as Conditions

Once the semantic and structural features are obtained from condition maps, we concatenate them with the features obtained by Eq. (5) along the last dimension:

$$\bar{\mathbf{f}}^C = \text{Concat}(\bar{\mathbf{f}}, \mathbf{f}_{sem}, \mathbf{f}_{str}). \quad (10)$$

The feature $\bar{\mathbf{f}}^C \in \mathbb{R}^{\frac{H}{r} \times \frac{W}{r} \times (D' + 2D)}$ is used to replace $\bar{\mathbf{f}}$ as the input of the first transformer block.

Though users can achieve controllability over inpainted images with the above two types of conditions, it is not flexible enough in the inference stage if users are always asked to provide these two types of conditions. Therefore, we introduce a placeholder embedding for each type of condition, which has the shape of $1 \times 1 \times D$ and is learned during the training stage. When a certain type of condition is absent, the corresponding placeholder embedding is repeated and expanded to the shape $\frac{H}{r} \times \frac{W}{r} \times D$ and used as the features to be concatenated in Eq. (10). With the help of placeholder embeddings, users are allowed to provide none, one, or both of these two types of conditions, making PUT more flexible in real-world applications.

In the training stage of UQ-Transformer, the classification loss in Eq. (6) is used and the condition features are replaced with their corresponding placeholder embeddings randomly with a probability of 0.3.

4 EXPERIMENTS

4.1 Datasets

The evaluation is conducted on FFHQ [17], Places2 [18], and ImageNet [19]. We use the original training and testing splits for Places2 and ImageNet. For FFHQ, we maintain the last 1K images for evaluation and use the others for training. Following ICT [10], 1K images are randomly chosen from the test split of ImageNet for evaluation, and the irregular masks provided by PConv [8] are used for both training and testing. While applying the pretrained transformer in PUT to downstream tasks, COCO [51] and LVIS [52] are used for the evaluation of object detection and segmentation.

4.2 Implementation Details

We set $r = 8$ and $r = 16$ for resolution 256×256 and 512×512 , respectively, making the encoder produce features that have the same spatial size 32×32 . To change the resolutions of features in the decoder, we adopt the nearest upsampling/downsampling. We train P-VQVAE with Adam [54], where the coefficients used for computing running averages of gradient and its square are set to 0 and 0.9. The batch size is set to 192 for FFHQ and Places2 and 384 for ImageNet. The learning rate is warmed up from 0 to $2e-4$ linearly in the first 5K iterations and then decayed with a cosine scheduler. For different datasets, P-VQVAEs are all optimized for 100 epochs. In our conference paper [48], the number of latent vectors is set to $K = 512$ and $K' = 512$, which are increased to $K = 8192$ and $K' = 1024$ in this paper. The Gumbel-Softmax relaxation [49] is adopted during the whole training procedure. Specifically, the Gumbel relaxation temperature is annealed from 20 to $1e-6$ over the first 5K iterations using a cosine annealing and the scale of added Gumbel noise is dropped from 1 to 0.1 after the 5K-th iteration.

The UQ-Transformer in this paper is modified from ViT-Base [55]: the convolution layer for patch embedding and the classification token for image classification are removed. For different datasets, we use UQ-Transformer with the same number of parameters, which differs from the settings in our conference paper [48] (see Table 4). Given the pretrained P-VQVAE, UQ-Transformer is optimized with AdamW [56]. The coefficients for computing running average and square of gradient are set to 0.9 and 0.95. The batch size is 192 for FFHQ and Places2 and 384 for ImageNet. The learning rate is increased from $1e-5$ to $1.5e-3$ linearly during the first 20K iterations. All models are trained to their convergence. We set D' to 256/768 for PUT with/without conditions to ensure that the hidden dimension of UQ-Transformer is the same as ViT-Base. For controllable image inpainting, we use the segmentation map predicted by Mask2Former [57] (with $C = 133$ known categories) and the sketch map predicted by DexiNed [58] to train the model. The number of unknown categories U is set to 20.

We compare PUT with several state-of-the-art methods. The method in our conference paper [48] is denoted as "PUT_{CVPR}". For a fair comparison, we directly use the pretrained models provided by the authors when available, otherwise, we train the models ourselves using the official codes and settings. Since existing inpainting methods do not support controllable inpainting, we compare PUT with

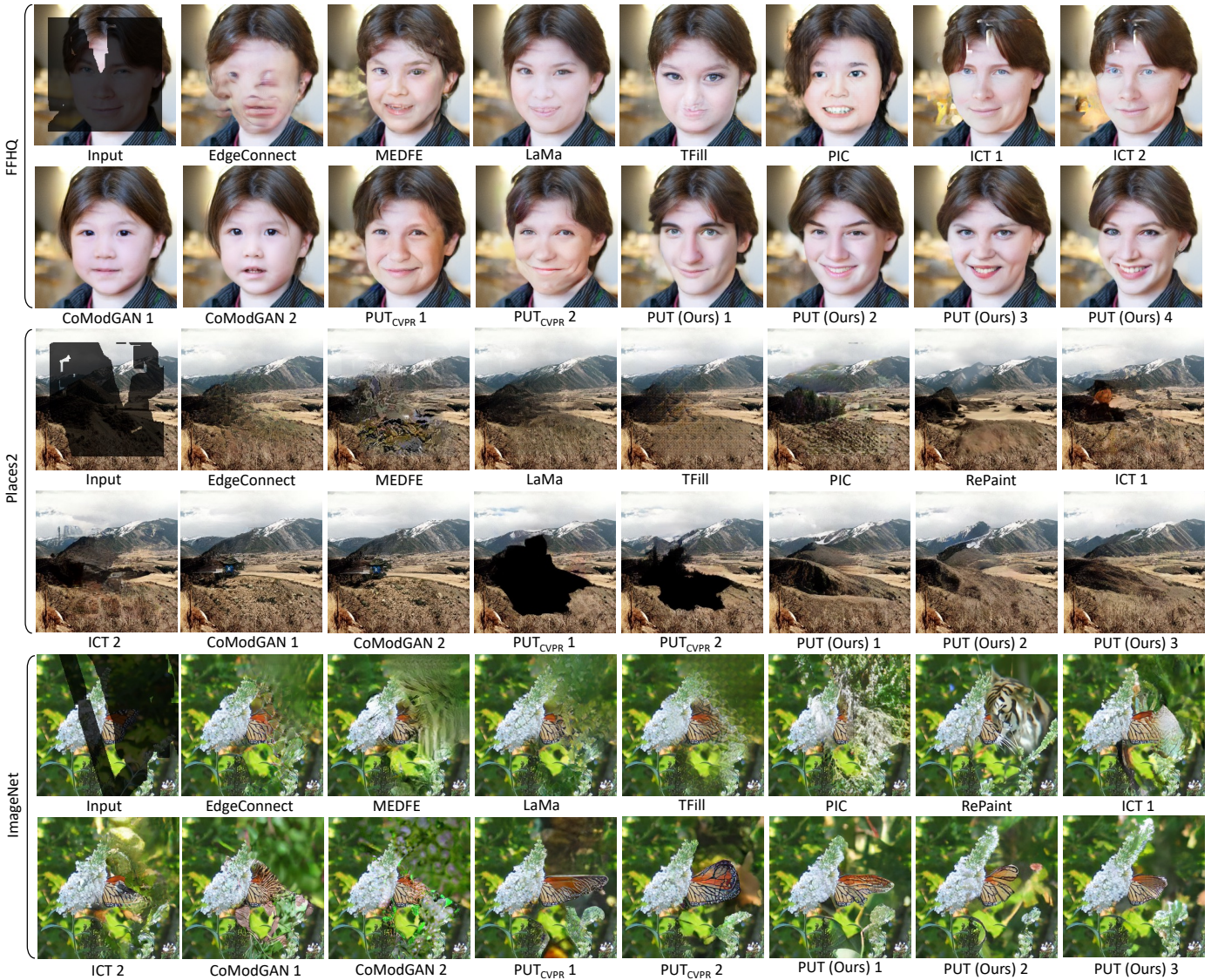


Fig. 5: Inpainting results produced by different methods on different datasets. The images produced by PUT are of higher diversity and visual quality.

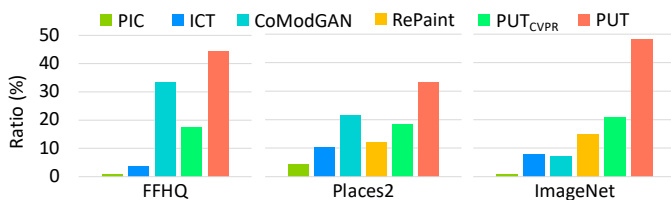


Fig. 6: The ratio of each method that is chosen as the rank 1st result by humans. Statistics are collected from 20 participants. Note that the diffusion model based RePaint [53] is not involved in the evaluation on FFHQ [17] since there is no available model. Reported on 256×256 resolution.

other methods without using conditions. The controllability of PUT is discussed and evaluated in Section 4.5.

4.3 Evaluation on 256×256 Resolution

The evaluated methods are EdgeConnect [9], MEDFE [59], TFill [60], PIC [43], ICT [10], RePaint [53] and PUT_{CVPR} [48].

Among these methods, the first three are deterministic methods, while the last four are pluralistic methods. Some recently proposed methods, including LaMa [41] (deterministic) and CoModGAN [45] (pluralistic), which are mainly designed for 512×512 resolution, are also modified to 256×256 resolution for more comparisons.

4.3.1 Qualitative Comparisons

The inpainting results on FFHQ [17], Places2 [18], and ImageNet [19] of different methods are shown in Fig. 5. Overall, PUT is more capable of catching the structure of the content in the image than other methods when most pixels are missing. It is clear that: 1) most existing methods perform better on monotonous datasets (e.g., FFHQ for faces and Places2 for natural scenes) than complex datasets (i.e., ImageNet), indicating their poor generalization ability. By contrast, our PUT generates vivid results for different cases and different datasets. 2) diverse and photorealistic results are produced by PUT. However, the results generated by

TABLE 1: Quantitative results for resolution 256×256 . PUT samples the tokens for all masked patches within one iteration for the comparison with deterministic methods (top group), but samples the tokens for 20 masked patches iteratively for the comparison with pluralistic methods (bottom group).

Dataset		FFHQ [17]			Places2 [18]			ImageNet [19]		
Mask Ratio (%)		20-40	40-60	10-60	20-40	40-60	10-60	20-40	40-60	10-60
FID ↓	EdgeConnect (ICCVW, 2019) [9]	12.949	26.217	16.961	20.180	34.965	23.206	27.821	63.768	39.199
	MEDFE (ECCV, 2020) [59]	13.999	26.252	17.061	28.671	46.815	32.494	40.643	93.983	54.854
	LaMa (WACV, 2022) [41]	9.757	18.648	13.786	20.268	33.216	22.599	18.988	45.051	26.854
	TFill (CVPR, 2022) [60]	11.340	19.486	12.984	19.512	34.022	23.753	24.739	50.670	32.342
	ICT (ICCV, 2021) [10]	10.442	23.946	15.363	19.309	33.510	23.331	23.889	54.327	32.624
	PUT _{CVPR} (CVPR, 2022) [48]	11.221	19.934	13.248	19.776	38.206	24.605	19.411	43.239	26.223
	PUT (Ours)	10.844	18.842	12.728	18.219	29.758	21.234	18.411	41.441	24.794
	PIC (CVPR, 2019) [43]	22.847	37.762	25.902	31.361	44.289	34.520	49.215	102.561	63.955
	CoModGAN (ICLR, 2021) [45]	10.102	17.770	12.236	20.804	33.931	25.367	29.414	64.020	38.652
	ICT (ICCV, 2021) [10]	13.536	23.756	16.202	20.900	33.696	24.138	25.235	55.598	34.247
	RePaint (CVPR, 2022) [53]	-	-	-	17.792	31.934	21.732	24.525	60.476	35.723
	PUT _{CVPR} (CVPR, 2022) [48]	12.784	21.382	14.554	19.617	31.485	22.121	21.272	45.153	27.648
	PUT (Ours)	11.891	19.458	13.805	19.028	29.122	21.158	19.956	40.329	25.642
	LPIPS ↓	EdgeConnect (ICCVW, 2019) [9]	0.0974	0.2055	0.1330	0.1217	0.2220	0.1470	0.1417	0.2531
MEDFE (ECCV, 2020) [59]		0.1080	0.1997	0.1355	0.1617	0.2760	0.1953	0.1826	0.3169	0.2219
LaMa (WACV, 2022) [41]		0.0743	0.1716	0.1104	0.1330	0.2260	0.1496	0.1147	0.2205	0.1463
TFill (CVPR, 2022) [60]		0.0904	0.1665	0.1331	0.1172	0.2036	0.1434	0.1292	0.2304	0.1601
ICT (ICCV, 2021) [10]		0.0814	0.1838	0.1219	0.1224	0.2231	0.1534	0.1263	0.2425	0.1636
PUT _{CVPR} (CVPR, 2022) [48]		0.0883	0.1647	0.1112	0.1224	0.2280	0.1555	0.1159	0.2257	0.1518
PUT (Ours)		0.0870	0.1605	0.1089	0.1223	0.2159	0.1505	0.1102	0.2163	0.1454
PIC (CVPR, 2019) [43]		0.1497	0.2660	0.1816	0.1889	0.2962	0.2129	0.2114	0.3510	0.2538
CoModGAN (ICLR, 2021) [45]		0.0867	0.1705	0.1126	0.1177	0.2170	0.1416	0.1479	0.2717	0.1857
ICT (ICCV, 2021) [10]		0.1001	0.1944	0.1276	0.1285	0.2306	0.1535	0.1348	0.2567	0.1752
RePaint (CVPR, 2022) [53]		-	-	-	0.1265	0.2394	0.1628	0.1310	0.2673	0.1767
PUT _{CVPR} (CVPR, 2022) [48]		0.0983	0.1818	0.1231	0.1265	0.2255	0.1569	0.1263	0.2409	0.1616
PUT (Ours)		0.0941	0.1712	0.1167	0.1252	0.2193	0.1532	0.1184	0.2256	0.1527
PSNR ↑		EdgeConnect (ICCVW, 2019) [9]	27.484	22.574	26.181	26.536	22.755	25.975	24.703	20.459
	MEDFE (ECCV, 2020) [59]	27.117	22.499	26.111	25.401	21.543	24.510	23.730	19.560	22.752
	LaMa (WACV, 2022) [41]	29.834	24.463	27.545	27.004	23.260	26.803	26.001	21.614	25.140
	TFill (CVPR, 2022) [60]	27.171	22.915	26.260	26.699	23.177	25.916	24.855	20.970	23.965
	ICT (ICCV, 2021) [10]	29.847	23.041	26.736	25.836	22.120	24.986	24.249	20.045	23.317
	PUT _{CVPR} (CVPR, 2022) [48]	28.356	24.125	27.473	26.580	22.945	25.749	25.721	21.551	24.726
	PUT (Ours)	28.538	24.200	27.616	26.220	22.579	25.442	25.736	21.504	24.719
	PIC (CVPR, 2019) [43]	25.157	20.424	24.093	24.073	20.656	23.469	22.921	18.368	21.623
	CoModGAN (ICLR, 2021) [45]	27.261	22.411	26.165	26.333	21.986	25.120	23.882	19.412	23.839
	ICT (ICCV, 2021) [10]	26.462	21.816	25.515	24.947	21.126	24.373	23.252	19.025	22.123
	RePaint (CVPR, 2022) [53]	-	-	-	25.146	20.899	24.136	23.268	18.380	22.067
	PUT _{CVPR} (CVPR, 2022) [48]	26.877	22.375	25.943	25.452	21.528	24.492	24.238	19.742	23.264
	PUT (Ours)	27.504	23.127	26.582	25.757	22.028	24.901	24.542	20.044	23.459
	SSIM ↑	EdgeConnect (ICCVW, 2019) [9]	0.941	0.826	0.899	0.881	0.734	0.840	0.882	0.714
MEDFE (ECCV, 2020) [59]		0.936	0.840	0.903	0.854	0.685	0.796	0.861	0.675	0.795
LaMa (WACV, 2022) [41]		0.963	0.887	0.923	0.887	0.750	0.852	0.906	0.759	0.857
TFill (CVPR, 2022) [60]		0.938	0.848	0.907	0.887	0.757	0.841	0.888	0.741	0.836
ICT (ICCV, 2021) [10]		0.964	0.863	0.917	0.870	0.723	0.819	0.876	0.711	0.818
PUT _{CVPR} (CVPR, 2022) [48]		0.953	0.888	0.908	0.885	0.756	0.840	0.904	0.772	0.838
PUT (Ours)		0.954	0.890	0.933	0.877	0.740	0.831	0.904	0.773	0.856
PIC (CVPR, 2019) [43]		0.910	0.769	0.865	0.824	0.648	0.775	0.842	0.623	0.766
CoModGAN (ICLR, 2021) [45]		0.939	0.840	0.904	0.875	0.713	0.811	0.866	0.685	0.803
ICT (ICCV, 2021) [10]		0.931	0.822	0.896	0.850	0.682	0.803	0.852	0.666	0.786
RePaint (CVPR, 2022) [53]		-	-	-	0.853	0.674	0.792	0.852	0.638	0.775
PUT _{CVPR} (CVPR, 2022) [48]		0.936	0.845	0.906	0.861	0.703	0.806	0.875	0.704	0.818
PUT (Ours)		0.944	0.863	0.916	0.869	0.722	0.818	0.882	0.721	0.826

other methods are full of artifacts, especially for the cases from ImageNet.

4.3.2 User Study

For the evaluation of subjective quality, a user study is conducted. Since PUT is mainly designed for pluralistic image inpainting, only pluralistic methods are evaluated. Specifically, we randomly sample 20 pairs of images and masks from the test set of each dataset. For each pair, we generate one inpainted image using each method and ask the participants to rank these images according to their photorealism from high to low. We calculate the ratio of each method among the rank 1st images. Results are shown

in Fig. 6. Our method takes up at least 30% of the rank 1st images and outperforms other baseline methods.

4.3.3 Quantitative Comparisons

We further demonstrate the superiority of PUT in terms of diversity and fidelity over other pluralistic methods. Specifically, the mean LPIPS distance [61] between pairs of randomly generated results for the same input image is calculated. Following ICT [10], five pairs per input image are generated. Meanwhile, the Fréchet Inception Distance (FID) [62] is also computed between the inpainted images and ground-truth images to reveal the fidelity of generated results. The curves of LPIPS and FID are shown in Fig. 8.

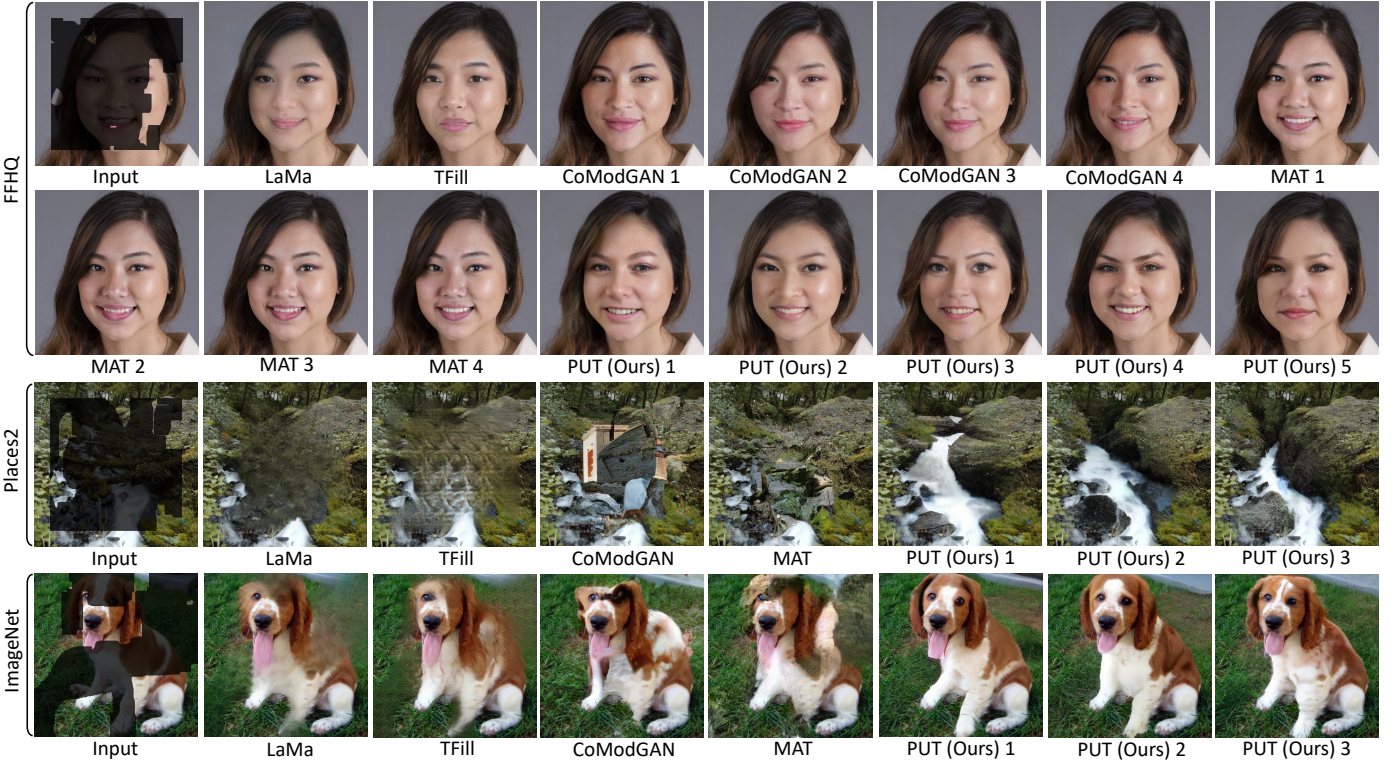


Fig. 7: Results produced by different methods. PUT generates more photorealism images than LaMa [41] and TFill [60], and produces more diverse results than CoModGAN [45] and MAT [46]. For Places2 and ImageNet, only one sample of CoModGAN and MAT is presented due to their low diversity and limited space. Shown at 512×512 resolution.

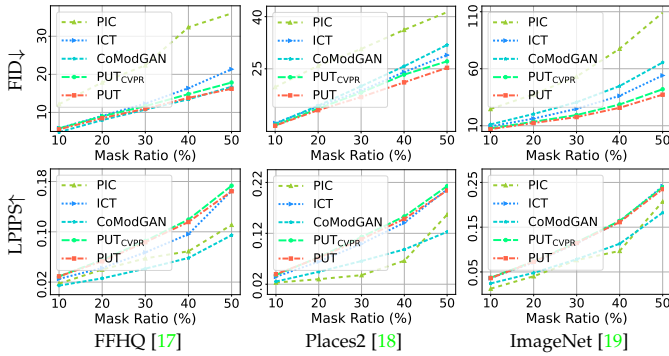


Fig. 8: Diversity and fidelity comparison between different pluralistic methods. RePaint [53] is not evaluated due to its slow inference speed (about 6 minutes per image). Reported on 256×256 resolution.

It can be seen that: 1) PUT achieves the best fidelity on Places2 [18] and ImageNet [19], especially for large areas of masked regions. For FFHQ [17], CoModGAN [45] achieves overall better fidelity (lower FID) than PUT. This is in accordance with our expectation since CoModGAN is implemented based on StyleGAN2 [47], which is a powerful face generator. 2) PUT achieves the best diversity (highest LPIPS) on all datasets. As ICT, PUT_{CVPR}, and PUT are all transformer based autoregressive methods, they have similar capabilities of generating diverse results. However, PUT samples the tokens for multiple masked patches (20, more exactly) per iteration, while ICT and PUT_{CVPR} sample the token for one masked patch per iteration. This difference

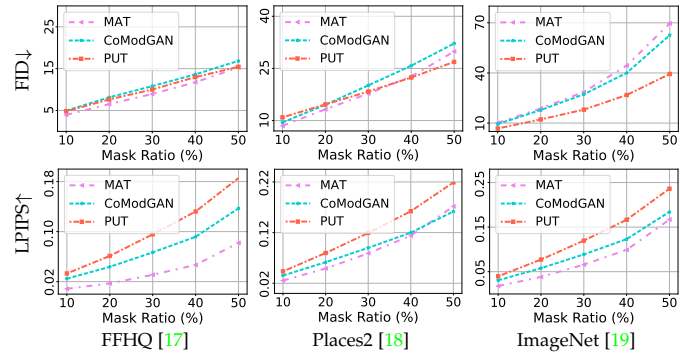


Fig. 9: Diversity and fidelity comparison between different pluralistic methods. Reported on 512×512 resolution.

makes PUT 20× faster during inference (Ref. Table 4).

In Table 1, we compare different methods in terms of several metrics. Only one recovered output is produced for each input. For the comparison with pluralistic methods, PUT performs the best in all metrics on ImageNet and achieves the best scores in almost all metrics on Places2. Specifically, the FID score of PUT on ImageNet with mask ratio 40%-60% is 15.269 lower than ICT and 4.824 lower than PUT_{CVPR}. Though CoModGAN achieves a better FID score on FFHQ than PUT, the FID score of CoModGAN on ImageNet is much poorer than PUT. This may be due to the inherent properties in the model structure of CoModGAN, which is similar to the powerful face generator StyleGAN2 [47]. For the comparisons with deterministic methods, PUT also achieves almost the best FID score on Places2 and ImageNet.

TABLE 2: Quantitative results for resolution 512×512 . PUT samples the tokens of all and 20 masked patches for comparison with deterministic and pluralistic methods, respectively. Gray results indicate more training data is used.

Dataset		FFHQ [17]			Places2 [18]			ImageNet [19]		
Mask Ratio (%)		20-40	40-60	10-60	20-40	40-60	10-60	20-40	40-60	10-60
FID↓	LaMa (WACV, 2022) [41]	9.523	18.876	11.765	<u>17.031</u>	31.182	<u>20.663</u>	18.754	44.579	26.633
	TFill (CVPR, 2022) [60]	12.050	21.186	14.099	24.619	40.502	28.448	27.163	58.695	36.314
	PUT (Ours)	10.255	18.694	12.239	20.156	31.159	22.710	18.619	42.459	25.452
	CoModGAN (ICLR, 2021) [45]	10.246	17.933	12.495	19.591	33.147	23.471	25.582	57.126	34.761
	MAT (CVPR, 2022) [46]	8.269	15.578	10.124	<u>17.850</u>	31.184	<u>21.655</u>	26.752	63.159	36.918
	PUT (Ours)	10.806	18.585	12.471	20.513	30.914	23.315	19.651	41.373	25.675
LPIPS↓	LaMa (WACV, 2022) [41]	0.1047	0.1964	0.1327	<u>0.1642</u>	<u>0.2339</u>	<u>0.1642</u>	0.1228	0.2332	0.1583
	TFill (CVPR, 2022) [60]	0.0942	0.2116	0.1462	0.1576	0.2650	0.1889	0.1528	0.2628	0.1860
	PUT (Ours)	<u>0.1089</u>	0.1944	0.1335	0.1927	0.2815	0.2193	0.1280	0.2357	0.1621
	CoModGAN (ICLR, 2021) [45]	0.1194	0.2146	0.1472	0.1462	0.2511	0.1772	0.1523	0.2709	0.1887
	MAT (CVPR, 2022) [46]	0.0942	0.1797	0.1200	<u>0.1351</u>	<u>0.2393</u>	<u>0.1668</u>	0.1552	0.2790	0.1928
	PUT (Ours)	0.1147	0.2039	0.1403	0.1969	0.2876	0.2303	0.1333	0.2429	0.1677
PSNR↑	LaMa (WACV, 2022) [41]	29.006	24.012	27.863	26.249	22.691	25.469	26.394	21.840	25.287
	TFill (CVPR, 2022) [60]	27.807	23.285	26.815	26.699	22.741	25.449	25.206	21.134	24.250
	PUT (Ours)	28.699	24.227	27.755	24.009	21.051	23.346	25.718	21.338	24.709
	CoModGAN (ICLR, 2021) [45]	27.325	22.439	26.220	24.776	<u>20.969</u>	23.886	24.223	19.659	23.114
	MAT (CVPR, 2022) [46]	28.270	23.375	27.218	<u>24.785</u>	<u>20.870</u>	<u>23.899</u>	24.249	19.798	23.255
	PUT (Ours)	27.700	23.109	26.724	23.240	20.555	22.800	24.814	20.405	23.763
SSIM↑	LaMa (WACV, 2022) [41]	0.937	0.837	0.901	0.869	<u>0.727</u>	<u>0.822</u>	0.898	0.752	0.845
	TFill (CVPR, 2022) [60]	0.923	0.817	0.887	0.887	0.722	0.817	0.876	0.726	0.824
	PUT (Ours)	0.936	0.853	0.908	0.769	0.637	0.723	0.890	0.750	0.841
	CoModGAN (ICLR, 2021) [45]	0.918	0.801	0.878	0.839	<u>0.676</u>	<u>0.785</u>	0.861	0.688	0.800
	MAT (CVPR, 2022) [46]	0.932	0.833	0.897	<u>0.840</u>	<u>0.676</u>	<u>0.785</u>	0.862	0.689	0.820
	PUT (Ours)	0.922	0.820	0.888	0.759	0.621	0.700	0.874	0.718	0.819

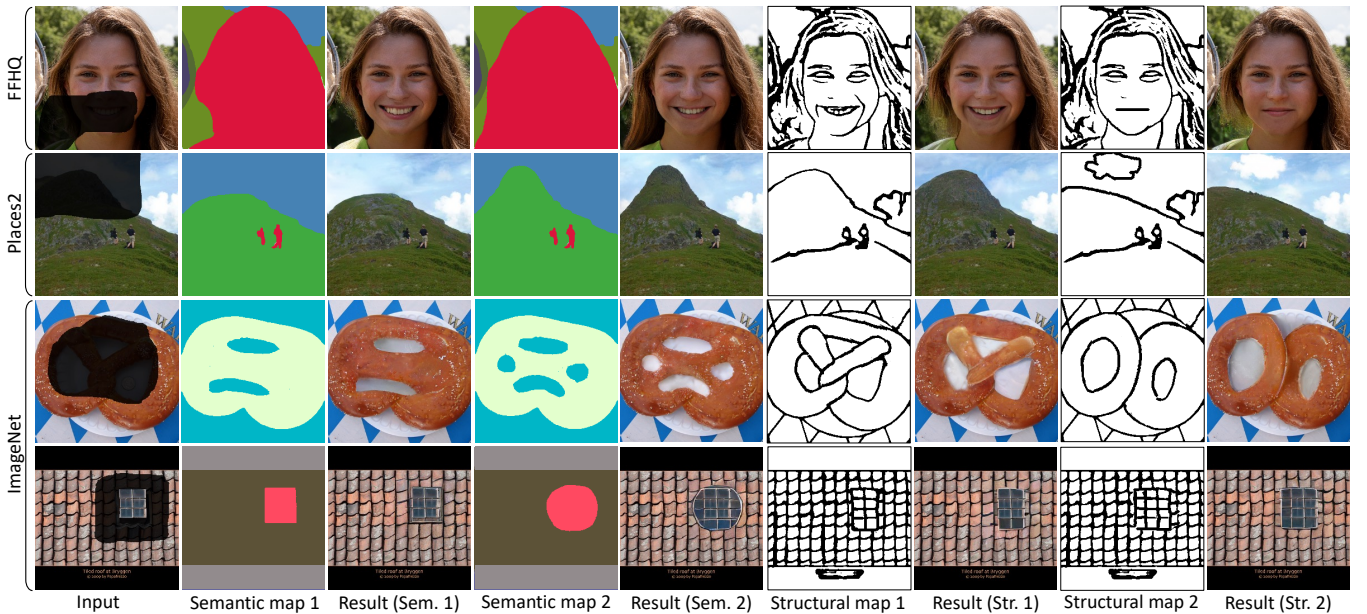


Fig. 10: Inpainted results with different conditions. PUT strictly follows different types of conditions. Shown at 256×256 .

4.4 Evaluation on 512×512 Resolution

As some recently proposed methods support image inpainting on 512×512 resolution, we also apply PUT to such resolution. The evaluated methods are LaMa [41], TFill [60], CoModGAN [45], and MAT [46]. Note that the models of LaMa, CoModGAN, and MAT on ImageNet are trained by ourselves since there are no available models.

4.4.1 Qualitative Comparisons

The inpainting results are shown in Fig. 7. Overall, PUT produces diverse and promising results on different datasets. Benefiting from StyleGAN2, both CoModGAN and MAT

produce impressive face images. However, their diversity is very limited. In addition, they fail to get plausible results on Places2 and ImageNet.

4.4.2 Quantitative Comparisons

Similar to the settings in Section 4.3.3, we compare different pluralistic methods in terms of fidelity and diversity in Fig. 9. Compared to MAT, PUT achieves comparable fidelity on FFHQ and Places2 but much higher diversity.

In Table 2, we present several metrics of different methods. Compared to deterministic methods, PUT achieves the best FID scores on different datasets when 40%-60%

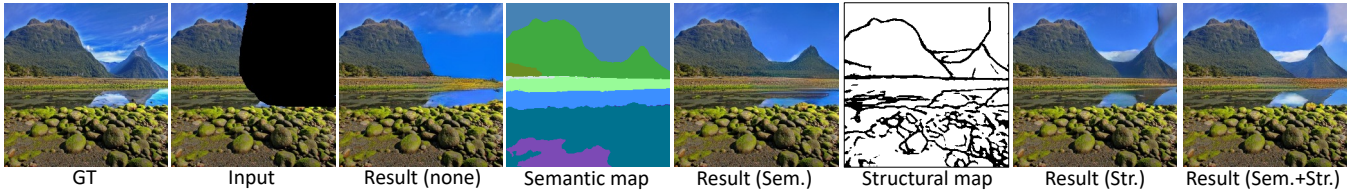


Fig. 11: The user-provided conditions can avoid some artifacts and make the results more desirable. Shown at 256×256 .

TABLE 3: Quantitative results of PUT with different conditions. Images are sampled within one iteration. Evaluated on 256×256 with mask ratio 10%-60%.

	Trained with conditions	Conditions	FFHQ [17]	Places2 [18]	ImageNet [19]
FID↓	×	none	12.728	21.234	24.794
		none	12.778	21.851	26.402
	✓	Sem.	12.340	20.403	23.729
		Str.	11.257	19.250	18.281
		Sem.+Str.	11.117	18.781	17.916
mIoU↑	×	none	0.7179	0.6911	0.5909
		none	0.7184	0.6786	0.5796
	✓	Sem.	0.7286	0.7133	0.6153
		Str.	0.7279	0.7083	0.6146
		Sem.+Str.	0.7338	0.7131	0.6201
F1 ↑	×	none	0.7796	0.7197	0.7682
		none	0.7785	0.7119	0.7638
	✓	Sem.	0.7881	0.7376	0.7793
		Str.	0.8237	0.7751	0.8207
		Sem.+Str.	0.8240	0.7763	0.8215

of pixels are masked. Compared to pluralistic methods, both CoModGAN and MAT perform overall better than PUT on FFHQ. We argue that the superiority of these two methods comes from the well-designed model structure in StyleGAN2 [47] for face generation. On the more complex dataset (*i.e.*, ImageNet), PUT performs much better than them on all metrics. In addition, PUT achieves comparable performances to CoModGAN and MAT on Places2, even though the number of training images of PUT (0.238M) is smaller than that of CoModGAN (8M) and MAT (1.8M).

4.5 Evaluation of Controllable Image Inpainting

In this section, we show the controllability of PUT with the user-provided semantic and structural maps. Without loss of generality, the experiments in this section are conducted on 256×256 resolution.

4.5.1 Qualitative Analysis

The visual results are shown in Fig. 10. As we can see, PUT follows the conditions provided by users, proving the superior controllability of PUT. For example, in the third scene, the donut is modified to have different shapes according to different semantic and structural maps. In Fig. 11, we show a case where the artifacts are avoided with more conditions. It can be seen that the result is over-smoothed when no condition is provided (Result (none)). With the help of the semantic map, the visual quality is greatly improved (Result (Sem.)). However, the mountain’s reflection in the water is unnatural. When PUT is conditioned on the structural map, the inpainted image (Result (str.)) follows the structural map but the generated content is still not perfect. Finally,

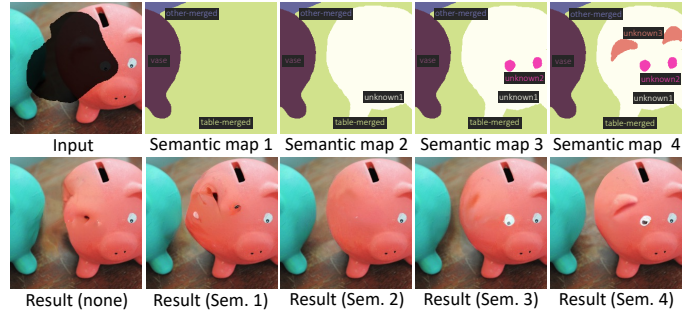


Fig. 12: The effectiveness of unknown category strategy. Semantic map 1 is obtained by Mask2Former [57]. Semantic maps 2-4 are manually added with 1-3 unknown categories. Shown at 256×256 .

when both semantic and structural guidances are given, the inpainting results are further improved (Result (Sem.+Str.)).

The effectiveness of the unknown category strategy is shown in Fig. 12. It can be seen that the segmentation model trained with a pre-defined closed-set of categories cannot recognize some objects correctly. Conditioned on an improper semantic map (Semantic map 1), PUT generates an artificial inpainted image (Result (Sem. 1)). However, when unrecognized objects (*e.g.*, piggy bank, eyes, ears) are labeled with unknown categories, images with better quality are produced.

4.5.2 Quantitative Analysis

As manually drawing the semantic and structural maps for all images in test splits is laborious and time-consuming, we use the maps obtained from the completed images to simulate user-provided maps for quantitative evaluation. To evaluate how well PUT follows the provided conditions, we get the mIoU (mean Intersection over Union)/F1 score between the provided segmentation/sketch maps and the segmentation/sketch maps obtained from inpainted images.

We first show the controllability of PUT with different conditions in Table 3. When no conditions are provided in the inference stage, comparable performances are achieved by two variants of PUT, *i.e.*, trained with and without conditions, demonstrating that the placeholder embeddings for different conditions have no negative effect on the inpainting quality. For the PUT trained with conditions, all metrics are improved even when only one type of condition is provided, demonstrating the effectiveness of our controllable design and the effectiveness of placeholder embeddings in handling the absence of conditions. Interestingly, the structural maps result in a better FID score than semantic maps since they contain more detailed textures. Compared

TABLE 4: The comparison of FLOPs, number of parameters and inference time. For ICT [10], PUT_{CVPR} [48] and PUT, these metrics of transformer and other components are shown separately since only the transformer need to be iteratively used for pluralistic image inpainting. Due to the various dependencies of different codes, it is hard to make a fair comparison of inference time. The used GPUs are provided for reference. Note that the Mask Ratio (MR) lies in the open interval (0,1).

Resolution	Method	Pluralistic	Parameters (M)	FLOPs (G)	Time (s/image)	Number of Iterations	GPU
256 × 256	EdgeConnect (ICCVW, 2019) [9]	×	20.5	122.6	0.024	1	TITAN Xp
	MEDFE (ECCV, 2020) [59]	×	124.3	138.0	0.127	1	TITAN Xp
	LaMa (WACV, 2022) [41]	×	22.9	42.9	0.029	1	RTX 3090
	TFill (CVPR, 2022) [60]	×	61.2	28.3	0.046	1	RTX 3090
	PIC (CVPR, 2019) [43]	×	5.7	36.2	0.035	1	TITAN Xp
	CoModGAN (ICLR, 2021) [45]	✓	75.5	14.8	0.038	1	TITAN Xp
	RePaint (CVPR, 2022) [53]	✓	527.2	1113.8×Iters.	0.079×Iters.	4570	RTX 3090
	FFHQ [17]		91.8+10.3	957.5×Iters.+62.0	0.073×Iters.+0.010	$\lceil MR \times 4096 \rceil$	
	ICT (ICCV, 2021) [10]	✓	106.2+10.3	283.6×Iters.+62.0	0.031×Iters.+0.010	$\lceil MR \times 1024 \rceil$	RTX 3090
	ImageNet [19]		422.4+10.3	791.5×Iters.+62.0	0.058×Iters.+0.010	$\lceil MR \times 1024 \rceil$	
	FFHQ [17]		90.5+7.6	217.2×Iters.+31.4	0.026×Iters.+0.015		
	PUT _{CVPR} (CVPR, 2022) [48]	✓	105.6+7.6	257.7×Iters.+31.4	0.031×Iters.+0.015	$\lceil MR \times 1024 \rceil$	RTX 3090
	ImageNet [19]		421.2+7.6	765.6×Iters.+31.4	0.058×Iters.+0.015		
	PUT, no condition, (Ours)	✓	87.3+10.6	193.2×Iters.+40.1	0.026×Iters.+0.016	$\lceil MR \times \frac{1024}{20} \rceil$	
	PUT, one condition, (Ours)	✓	87.3+11.2	193.2×Iters.+40.6	0.026×Iters.+0.018	$\lceil MR \times \frac{1024}{20} \rceil$	RTX 3090
PUT, two conditions, (Ours)	✓	87.3+11.8	193.2×Iters.+41.1	0.026×Iters.+0.020	$\lceil MR \times \frac{1024}{20} \rceil$		
512 × 512	LaMa (WACV, 2022) [41]	×	25.8	171.3	0.033	1	RTX 3090
	TFill (CVPR, 2022) [60]	×	104.4	50.5	0.074	1	RTX 3090
	CoModGAN (ICLR, 2021) [45]	✓	76.1	20.2	0.061	1	TITAN Xp
	MAT(CVPR, 2022) [46]	✓	58.7	212.0	0.065	1	RTX 3090
	PUT (Ours)	✓	87.3+20.5	193.2×Iters.+184.2	0.026×Iters.+ 0.018	$\lceil MR \times \frac{1024}{20} \rceil$	RTX 3090

TABLE 5: The effectiveness of unknown category strategy. Evaluated on 256 × 256 with mask ratio 10%-60%.

Configuration	FFHQ [17]		Places2 [18]		ImageNet [19]	
	FID↓	PSNR↑	FID↓	PSNR↑	FID↓	PSNR↑
Sem. ¹³³	12.340	27.980	20.403	26.066	23.729	25.211
Sem. ¹¹³	13.074	27.400	20.927	25.999	24.877	24.983
Sem. ¹¹³ +Unk.	12.343	27.977	20.387	26.066	23.674	25.207

to only giving one type of condition, PUT achieves better metrics when two types of conditions are both utilized.

To qualitatively show the effectiveness of the unknown category strategy, we compare the models trained with different settings, including using all the categories recognized by Mask2Former [57] (denoted as Sem.¹³³), removing 20 categories (denotes as Sem.¹¹³) recognized by Mask2Former, and using 20 unknown categories to substitute the removed categories (denoted as Sem.¹¹³+Unk.). Only the FID and PSNR metrics between inpainted and ground-truth images are evaluated. The mIoU is not used since the sets of categories in these three settings are different. Results are shown in Table 5. Compared with Sem.¹³³, Sem.¹¹³ achieves inferior performance on different metrics. When assisted with unknown categories, those unrecognized categories can be labeled with unknown categories, helping PUT inpaint images with better quality (Sem.¹¹³ vs Sem.¹¹³+Unk.).

4.6 FLOPs, Parameters and Inference Time

From the results presented in Table 4, we can see that for different methods, the FLOPs and the number of parameters are not constrained to be the same. For pluralistic methods, diffusion model based (e.g., RePaint) and transformer based autoregressive (like ICT, PUT_{CVPR} and PUT) solutions need several iterations to get diverse results, resulting in larger FLOPs and longer inference time. Compared with ICT and PUT_{CVPR}, PUT has the smallest number of parameters and

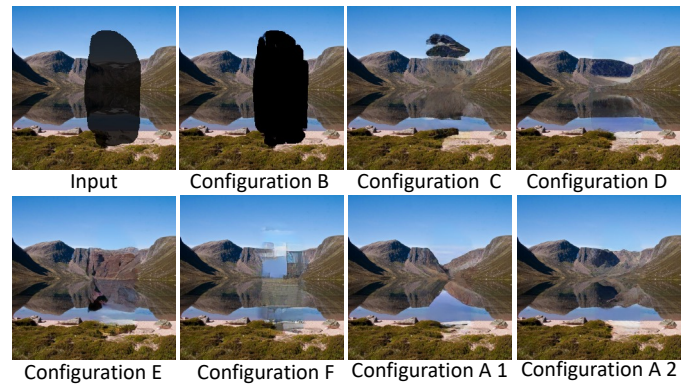


Fig. 13: Inpainted results under different configurations on Places2 [18].

takes the least number of iterations, resulting in a much faster inference speed and much fewer FLOPs. For example, the number of iterations of PUT is about 5.0% of ICT and PUT_{CVPR} and is at most 1.1% of RePaint.

4.7 Discussions

In this section, we provide some discussions on the design of PUT and the potential of applying the pretrained transformer in PUT to downstream tasks. Without loss of generality, the PUT trained without conditions is evaluated.

4.7.1 Effectiveness of Main Components

We first show the effectiveness of the patch-based encoder, dual-codebook, multi-scale guided decoder and un-quantized transformer. To this end, different configurations are designed. Results are shown in Table 6 and Fig. 13.

Configuration A is the default setting in our conference paper [48]. We first replace the patch-based encoder with

TABLE 6: Quantitative results of different settings. For PVQVAE, the numbers of latent vectors in e and e' both are set to 512 and the Gumbel-softmax relaxation is not used in the training stage. For UQ-Transformer, the mask embedding is not introduced. Images are sampled with $\mathcal{K}_1 = 1$ and $K_2 = 50$. Evaluated on 256×256 resolution with mask ratio 10%-60%.

Identifier	Configuration	FFHQ [17]				Places2 [18]			
		FID↓	LPIPS↓	PSNR↑	SSIM↑	FID↓	LPIPS↓	PSNR↑	SSIM↑
A	PUT in our conference paper [48]	14.554	0.1231	25.943	0.914	22.121	0.1569	24.492	0.806
B	A w/o Patched-based encoder	173.351	0.3822	12.360	0.445	179.294	0.3895	11.799	0.373
C	A w/o Dual-codebook	13.960	0.1201	25.903	0.906	28.634	0.1808	23.600	0.776
D	A w/o Guidance from reference branch in decoder	16.469	0.1378	25.547	0.906	25.084	0.1773	24.185	0.798
E	A w/o Un-quantized inputs to UQ-Transformer	26.098	0.1654	22.879	0.843	75.625	0.2383	19.429	0.652
F	A w/o Random quantization during training	54.879	0.2055	23.174	0.820	44.588	0.2075	23.353	0.763

TABLE 7: Quantitative results of different methods. We set $\mathcal{K}_1 = 1$ and increase \mathcal{K}_2 from 50 to 200 when the number of latent vectors in e is increased from 512 to 8192. Except for the mentioned difference between different configurations, others remain the same. Evaluated at 256×256 resolution with mask ratio 10%-60%.

Identifier	Configuration			Parameters of UQ-Transformer	FFHQ [17]				Parameters of UQ-Transformer	Places2 [18]			
	Number of latent vectors K	Gumbel-softmax relaxation	Mask Embedding		FID↓	LPIPS↓	PSNR↑	SSIM↑		FID↓	LPIPS↓	PSNR↑	SSIM↑
A	512	×	×	90.5M	14.554	0.1231	25.943	0.914	105.6M	22.121	0.1569	24.492	0.806
G	512	×	×	87.3M	14.764	0.1238	25.916	0.905	87.3M	22.696	0.1595	24.448	0.805
H	8192	×	×	87.3M	14.135	0.1214	26.038	0.908	87.3M	23.921	0.1553	24.535	0.808
I	8192	✓	×	87.3M	13.887	0.1196	26.196	0.912	87.3M	24.179	0.1599	24.413	0.808
J	8192	✓	✓	87.3M	13.658	0.1174	26.321	0.914	87.3M	21.538	0.1553	24.521	0.813

a normal CNN based encoder, which is implemented with convolution layers (Configuration B). The model performs the worst in all metrics, demonstrating the effectiveness of the non-overlapping patch partition design. Within CNN based encoder, the input images are processed in a sliding window manner, introducing the interaction between masked and unmasked regions, which is fatal to the transformer for the prediction of masked regions.

Configuration C removes the codebook e' from P-VQVAE. The only difference between configurations A and C is the training of P-VQVAE with one or two codebooks since the codebook e' is not used in the inference stage. P-VQVAE learns more discriminative features for masked and unmasked patches with the help of dual-codebook. Interestingly, the model with codebook e' indeed performs better than the model without it, except for the FID and LPIPS scores on FFHQ. We speculate that face generation is much easier because all faces share a similar structure. As we can see in Fig. 13, without the help of codebook e' , the model sometimes predicts *black* patches, which are similar to those patches containing missing pixels. By contrast, the dual-codebook helps PUT achieve overall better performance.

Configuration D removes the guidance of the reference branch, which means that the model constructs the inpainted image without referring to the input masked image, leading to inferior performance in terms of all metrics. With the help of multi-scale guidance from the reference branch, some useful textures can be recovered from the unmasked regions in the reference image. As we can see in Fig. 13, the result constructed without referring to the input image is over-smoothed and unnatural.

Configuration E feeds the transformer with quantized vectors rather than the original feature vectors from the encoder, which performs much poorer in all metrics than configuration A. Without quantizing feature vectors to discrete representations, no information loss happens in this step, which helps the transformer to understand complex content and maintain the inherent meaningful textures in

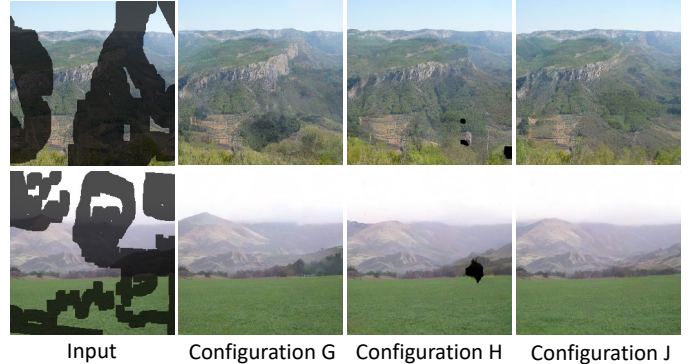


Fig. 14: Inpainted results under different configurations on Places2 [18]. More details about these configurations please refer to Table 7. Shown at 256×256 .

the input image. However, the training of the transformer should be carefully designed by randomly quantizing the input feature vectors since only quantized vectors can be obtained for masked regions at the inference stage. The effectiveness of such random quantization during training is obvious while comparing configuration A with F.

4.7.2 Discussion on Latent Vectors and Mask Embedding

Here, we show the effectiveness of mask embedding and the learning of more latent vectors with Gumbel-softmax relaxation. Results are shown in Table 7. We first switch UQ-Transformer in configuration A to a lighter one, which is implemented based on ViT-Base [55]. The performance drops slightly when a lighter UQ-Transformer is used.

Interestingly, when the number of latent vectors is increased from 512 to 8192, no matter whether the Gumbel-softmax relaxation is adopted (configuration I) or not (configuration H), the model achieves better performance on FFHQ [17], but inferior performance on Places2 [18]. However, the performance on both datasets is boosted with the help of mask embedding (configuration J). Here, we give an

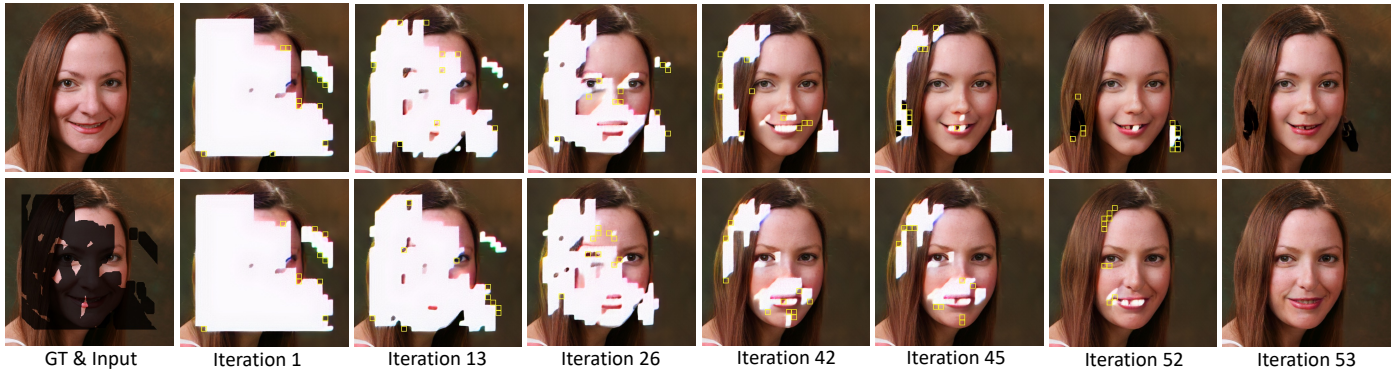


Fig. 15: Top: Artifacts produced by PUT without the help of mask embedding. Bottom: Vivid results produced by PUT with the help of mask embedding. The intermediate images are reconstructed by replacing the remanent masked tokens with a *white* token for better comparison. We set $\mathcal{K}_1 = 10$ and $\mathcal{K}_2 = 200$. The patches marked by yellow boxes are those inpainted patches at that iteration. Shown at 512×512 resolution.

TABLE 8: The impact of \mathcal{K}_1 . Except that the last row (marked by \sharp) is evaluated with $\mathcal{K}_2=1$, others are evaluated with $\mathcal{K}_2 = 200$. Time consumption is averaged by the number of all images in the test split. Reported on 256×256 resolution.

Mask Ratio	20%-40%					40%-60%					10%-60%				
	Metrics		FFHQ [17]		Time	FFHQ [17]		Places2 [18]		Time	FFHQ [17]		Places2 [18]		Time
	FID \downarrow	LPIPS \downarrow	FID \downarrow	LPIPS \downarrow		FID \downarrow	LPIPS \downarrow	FID \downarrow	LPIPS \downarrow		FID \downarrow	LPIPS \downarrow	FID \downarrow	LPIPS \downarrow	
\mathcal{K}_1					s/image										
1	12.186	0.0948	19.567	0.1270	7.822	19.157	0.1717	30.152	0.2222	11.453	13.658	0.1174	21.293	0.1553	8.849
5	12.053	0.0945	19.654	0.1263	1.584	19.691	0.1718	28.893	0.2208	2.295	13.740	0.1169	21.612	0.1544	1.777
20	11.891	0.0944	19.028	0.1253	0.415	19.458	0.1712	29.122	0.2193	0.587	13.805	0.1167	21.158	0.1532	0.464
100	12.098	0.0938	18.678	0.1242	0.105	20.402	0.1719	29.130	0.2173	0.137	14.137	0.1165	21.075	0.1523	0.116
All	12.181	0.9306	18.219	0.1223	0.042	23.510	0.1765	29.758	0.2160	0.043	15.006	0.1176	21.234	0.1505	0.043
All \sharp	10.844	0.0870	19.384	0.1235		18.842	0.1605	36.566	0.2244		12.728	0.1088	23.700	0.1542	

TABLE 9: The accuracy and probability of predicted tokens. Acc@MaxProb is the accuracy of tokens that with maximum probabilities. Prob@GT is the mean of those probabilities that correspond to ground-truth tokens. Evaluated at 512×512 with $\mathcal{K}_1 = 1$, $\mathcal{K}_2 = 200$ and mask ratio 10%-60%.

	w/o mask embedding		with mask embedding	
	Acc@MaxProb	Prob@GT	Acc@MaxProb	Prob@GT
FFHQ [17]	24.0%	0.172	24.4%	0.182
Places2 [18]	27.1%	0.201	28.0%	0.220

explanation of why the model achieves poorer performance on Places2 with more latent vectors even though the reconstruction capability of patch-based auto-encoder is greatly improved (FID/PSNR are improved from 35.183/23.560 to 33.810/24.594). The performance drop mainly comes from the artifacts: some unnatural *black* pixels are easily produced when the input image contains some natural black pixels (for example, the images produced by PUT_{CVPR} [48] in Fig. 5 on Places2). Different from photos of faces in FFHQ, textures or patterns in pictures taken from natural scenes sometimes contain scattered black pixels, for example, mountains and grasses. Such scattered black pixels are more easily recognized by PUT when more latent vectors are learned, making the transformer predict black pixels more often. Two examples are shown in Fig. 14. Such artifacts become more severe when applying PUT to higher resolutions. An example from FFHQ with resolution 512×512 is shown in Fig. 15. But when mask embedding is introduced (configuration J), PUT is greatly boosted.

In Table 9, we show the accuracy of predicted tokens and the probability scores for ground-truth tokens. With the help

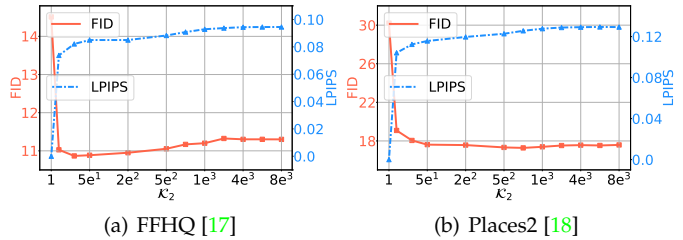


Fig. 16: LPIPS and FID curves with respect to \mathcal{K}_2 on different datasets when $\mathcal{K}_1 = 1$. Evaluated at 256×256 resolution with mask ratio 10%-60%.

of mask embedding, the transformer predicts the ground-truth tokens with a higher frequency (Acc@MaxProb) and a higher confidence (Prob@GT).

4.7.3 Discussions on Sampling Strategy

The impact of \mathcal{K}_2 when $\mathcal{K}_1 = 1$ is shown in Fig. 16. To get the diversity of inpainted images, five pairs of results for each input are generated to calculate the mean LPIPS [61] score. Meanwhile, the fidelity between all generated results and ground-truth images is also obtained. As we can see, when \mathcal{K}_2 is large enough ($\mathcal{K}_2 \geq 50$), the diversity and fidelity are saturated, which means PUT is not sensitive to the value of \mathcal{K}_2 . However, when \mathcal{K}_2 is too small ($\mathcal{K}_2 < 10$), PUT loses the capability of diversity and fidelity. We set $\mathcal{K}_2 = 200$ as default to balance the diversity and fidelity.

To evaluate the influence of \mathcal{K}_1 , we generate one result for each input. The LPIPS and FID scores between generated images and ground-truth images are calculated. Results are

TABLE 10: Applying pretrained transformers to downstream tasks. RL: Representation learning. GM: Generative modeling.

Methods	Pretraining details		Inpainting	Classification		Object detection and instance segmentation				
	Task	Epochs/ Batch size	ImageNet [19] FID↓	Resolution/ Patch size	ImageNet [19] Acc@1↑	Resolution/ Patch size	COCO [51]		LVIS [52]	
							AP ^{box} ↑	AP ^{mask} ↑	AP ^{box} ↑	AP ^{mask} ↑
Random [36]	-	-	-	224/16	82.3	1024/16	38.0	34.7	25.1	24.7
MAE (CVPR,2022) [36]		1600/4096	63.911	224/16	83.6		51.3	45.7	38.8	36.9
SimMIM (CVPR,2022) [63]	RL	800/2048	69.873	224/16	83.8	1024/16	49.7	44.2	36.5	34.8
BEiT (ICLR,2022) [35]		800/2048	127.913	224/16	83.2		48.4	43.0	35.8	34.3
MAGE (CVPR,2023) [37]	RL + GM	1600/4096	145.952	256/16	82.5		46.0	40.1	32.9	29.7
PUT, 512 × 512, (Ours)		300/384	25.452	224/16	82.7	1024/16	48.1	42.5	34.5	32.6
PUT, 256 × 256, (Ours)	Inpainting	300/384	24.794	224/16	82.9		49.0	43.5	35.4	33.3

shown in Table 8. We can find that: 1) The time consumption is less if PUT takes fewer iterations (*i.e.*, with a larger \mathcal{K}_1). 2) The impact of \mathcal{K}_1 on the quality of inpainted images is limited, which means PUT is somewhat robust to different values of \mathcal{K}_1 . 3) When inpainting an image within one iteration and setting \mathcal{K}_2 to 200 (denoted as *All*), PUT achieves worse performance on FFHQ when the mask ratio is large (*e.g.*, 40%-60%). However, such a phenomenon is not observed on Places2. The reason is that the faces in FFHQ are more structured than natural scene pictures in Places2. When the tokens for masked patches are sampled from top-200 elements independently, the structure of faces is destroyed. 4) In contrast to the aforementioned phenomenon, when the tokens for masked patches are sampled at one iteration with $\mathcal{K}_2 = 1$ (denoted as *All^h*), PUT performs much better on FFHQ but much worse on Places2. The reason is that the inpainted images are over-smoothed. Such smoothness is acceptable for faces but unnatural for natural scene pictures.

For iteratively image inpainting, we set $\mathcal{K}_1 = 20$, $\mathcal{K}_2 = 200$ for different datasets. For image inpainting within one iteration ($\mathcal{K}_1 = All$), we set $\mathcal{K}_2 = 1$ for FFHQ and ImageNet and $\mathcal{K}_2 = 200$ for Places2.

4.7.4 Comparison with Masked Image Modeling Methods

Finally, we compare PUT with some popular MIM methods for representation learning, including MAE [36], BEiT [35], SimMIM [63] and MAGE [37]. Among them, MAGE tries to unify generative modeling with representation learning. Results are shown in Table 10. For inpainting, the masked images (with a mask ratio ranging from 10%-60%) are fed into the pretrained models. For classification, the results of compared methods are extracted from their papers while the results of PUT are obtained through finetuning it on ImageNet for 200 epochs. For object detection and instance segmentation, all results are produced by us using the codes of ViTDet [64] through optimizing different methods for 50 epochs. The first kernel in 256×256 pretrained PUT model is interpolated to adapt to handle 16×16 image patches.

Overall, the methods that have image synthesis capability, *e.g.*, PUT and MAGE, are inferior to those methods that are dedicated to representation learning when applied to downstream tasks. However, PUT is much superior to MAGE and comparable to BEiT even though it is designed for image inpainting rather than representation learning. For the task of image inpainting, MAGE and BEiT perform much worse than other methods. The reason is that similar convolution-based auto-encoders in configuration B (Ref. Table 6) are adopted to provide the quantized discrete tokens [36], [63], demonstrating the effectiveness of P-VQVAE for image inpainting.

5 CONCLUSIONS AND LIMITATIONS

In this paper, we present a novel method, PUT, for pluralistic image inpainting. PUT consists of two main components: 1) patch-based auto-encoder (P-VQVAE) and 2) unquantized transformer (UQ-Transformer). With the help of P-VQVAE and UQ-Transformer, PUT processes the original high-resolution image without quantization. Such practice preserves the information contained in the input image as much as possible. Experimental results demonstrate the superiority of PUT, including fidelity and diversity, especially for large masked regions and complex scenes.

The main limitations of PUT include: 1) Inference time for generating diverse results. Though the inference time has been greatly reduced with the multi-token sampling strategy, PUT still needs several iterations to inpaint one image. However, it is a common issue of existing transformer based autoregressive methods [10], [15], [16]. 2) Generalization of image resolution. UQ-Transformer is sensitive to the length of sequence since it is trained with a fixed number of image patches and position embeddings. It may be solved by dynamically changing the resolution of input images during the training stage and using more flexible position embeddings [29]. We leave these to our future work.

Acknowledgements: This work was supported by the National Natural Science Foundation of China (62331006, 62171038, and 62088101), and the Fundamental Research Funds for the Central Universities.

REFERENCES

- [1] H. Qiu, C. Xiao, L. Yang, X. Yan, H. Lee, and B. Li, "Semanticadv: Generating adversarial examples via attribute-conditioned image editing," in *ECCV*, 2020, pp. 19–37. **1**
- [2] X. Zhan, X. Pan, B. Dai, Z. Liu, D. Lin, and C. C. Loy, "Self-supervised scene de-occlusion," in *CVPR*, 2020, pp. 3784–3792. **1**
- [3] C. Barnes, E. Shechtman, A. Finkelstein, and D. B. Goldman, "Patchmatch: A randomized correspondence algorithm for structural image editing," *ACM Trans. Graph.*, vol. 28, no. 3, p. 24, 2009. **1, 2**
- [4] Z. Tan, D. Chen, Q. Chu, M. Chai, J. Liao, M. He, L. Yuan, G. Hua, and N. Yu, "Efficient semantic image synthesis via class-adaptive normalization," *IEEE Trans. Pattern Anal. Mach. Intell.*, 2021. **1**
- [5] Y. Matsushita, E. Ofek, W. Ge, X. Tang, and H.-Y. Shum, "Full-frame video stabilization with motion inpainting," *IEEE Trans. Pattern Anal. Mach. Intell.*, vol. 28, no. 7, pp. 1150–1163, 2006. **1**
- [6] M. Bertalmio, L. Vese, G. Sapiro, and S. Osher, "Simultaneous structure and texture image inpainting," *IEEE Trans. Image Process.*, vol. 12, no. 8, pp. 882–889, 2003. **1**
- [7] A. Criminisi, P. Pérez, and K. Toyama, "Region filling and object removal by exemplar-based image inpainting," *IEEE Trans. Image Process.*, vol. 13, no. 9, pp. 1200–1212, 2004. **1**
- [8] G. Liu, F. A. Reda, K. J. Shih, T.-C. Wang, A. Tao, and B. Catanzaro, "Image inpainting for irregular holes using partial convolutions," in *ECCV*, 2018, pp. 85–100. **1, 3, 6**

- [9] K. Nazeri, E. Ng, T. Joseph, F. Qureshi, and M. Ebrahimi, "Edgeconnect: Structure guided image inpainting using edge prediction," in *ICCV*, 2019, pp. 0–0. [1](#), [3](#), [7](#), [8](#), [12](#)
- [10] Z. Wan, J. Zhang, D. Chen, and J. Liao, "High-fidelity pluralistic image completion with transformers," in *ICCV*, 2021, pp. 4692–4701. [1](#), [2](#), [3](#), [4](#), [5](#), [6](#), [7](#), [8](#), [12](#), [15](#)
- [11] Y. Yu, F. Zhan, R. Wu, J. Pan, K. Cui, S. Lu, F. Ma, X. Xie, and C. Miao, "Diverse image inpainting with bidirectional and autoregressive transformers," *arXiv:2104.12335*, 2021. [1](#), [2](#), [3](#)
- [12] N. Carion, F. Massa, G. Synnaeve, N. Usunier, A. Kirillov, and S. Zagoruyko, "End-to-end object detection with transformers," in *ECCV*, 2020, pp. 213–229. [1](#)
- [13] X. Dong, J. Bao, D. Chen, W. Zhang, N. Yu, L. Yuan, D. Chen, and B. Guo, "Cswin transformer: A general vision transformer backbone with cross-shaped windows," in *CVPR*, 2022, pp. 12 124–12 134. [1](#), [2](#)
- [14] M. Chen, A. Radford, R. Child, J. Wu, H. Jun, D. Luan, and I. Sutskever, "Generative pretraining from pixels," in *ICML*, 2020, p. 1691–1703. [1](#), [2](#)
- [15] P. Esser, R. Rombach, and B. Ommer, "Taming transformers for high-resolution image synthesis," in *CVPR*, 2021, pp. 12 873–12 883. [1](#), [2](#), [3](#), [4](#), [5](#), [15](#)
- [16] A. Ramesh, M. Pavlov, G. Goh, S. Gray, C. Voss, A. Radford, M. Chen, and I. Sutskever, "Zero-shot text-to-image generation," *arXiv:2102.12092*, 2021. [1](#), [2](#), [4](#), [5](#), [15](#)
- [17] T. Karras, S. Laine, and T. Aila, "A style-based generator architecture for generative adversarial networks," in *CVPR*, 2019, pp. 4401–4410. [2](#), [3](#), [6](#), [7](#), [8](#), [9](#), [10](#), [11](#), [12](#), [13](#), [14](#)
- [18] B. Zhou, A. Lapedriza, A. Khosla, A. Oliva, and A. Torralba, "Places: A 10 million image database for scene recognition," *IEEE Trans. Pattern Anal. Mach. Intell.*, vol. 40, no. 6, pp. 1452–1464, 2017. [2](#), [6](#), [7](#), [8](#), [9](#), [10](#), [11](#), [12](#), [13](#), [14](#)
- [19] J. Deng, W. Dong, R. Socher, L.-J. Li, K. Li, and L. Fei-Fei, "Imagenet: A large-scale hierarchical image database," in *CVPR*, 2009, pp. 248–255. [2](#), [3](#), [6](#), [7](#), [8](#), [9](#), [10](#), [11](#), [12](#), [15](#)
- [20] G. E. Hinton and R. S. Zemel, "Autoencoders, minimum description length, and helmholtz free energy," *NeurIPS*, vol. 6, pp. 3–10, 1994. [2](#)
- [21] S. Rifai, G. Mesnil, P. Vincent, X. Muller, Y. Bengio, Y. Dauphin, and X. Glorot, "Higher order contractive auto-encoder," in *ECML-PKDD*, 2011, pp. 645–660. [2](#)
- [22] R. Min, *A non-linear dimensionality reduction method for improving nearest neighbour classification*, 2005. [2](#)
- [23] D. P. Kingma and M. Welling, "Auto-encoding variational bayes," *arXiv:1312.6114*, 2013. [2](#)
- [24] A. Van Oord, N. Kalchbrenner, and K. Kavukcuoglu, "Pixel recurrent neural networks," in *ICML*, 2016, pp. 1747–1756. [2](#)
- [25] A. v. d. Oord, N. Kalchbrenner, O. Vinyals, L. Espeholt, A. Graves, and K. Kavukcuoglu, "Conditional image generation with pixelcnn decoders," in *NeurIPS*, 2016, pp. 4797–4805. [2](#)
- [26] A. van den Oord, O. Vinyals, and K. Kavukcuoglu, "Neural discrete representation learning," in *NeurIPS*, 2017, pp. 6309–6318. [2](#), [3](#), [4](#)
- [27] S. Gu, D. Chen, J. Bao, F. Wen, B. Zhang, D. Chen, L. Yuan, and B. Guo, "Vector quantized diffusion model for text-to-image synthesis," in *CVPR*, 2022. [2](#)
- [28] A. Razavi, A. van den Oord, and O. Vinyals, "Generating diverse high-fidelity images with vq-vae-2," in *NeurIPS*, 2019, pp. 14 866–14 876. [2](#), [3](#)
- [29] A. Vaswani, N. Shazeer, N. Parmar, J. Uszkoreit, L. Jones, A. N. Gomez, L. Kaiser, and I. Polosukhin, "Attention is all you need," *NeurIPS*, vol. 30, 2017. [2](#), [15](#)
- [30] X. Dong, J. Bao, T. Zhang, D. Chen, W. Zhang, L. Yuan, D. Chen, F. Wen, and N. Yu, "Peco: Perceptual codebook for bert pre-training of vision transformers," in *AAAI*, 2023. [2](#)
- [31] R. Wang, D. Chen, Z. Wu, Y. Chen, X. Dai, M. Liu, Y.-G. Jiang, L. Zhou, and L. Yuan, "Bevt: Bert pretraining of video transformers," in *CVPR*, 2022, pp. 14 733–14 743. [2](#)
- [32] L. Yuan, D. Chen, Y.-L. Chen, N. Codella, X. Dai, J. Gao, H. Hu, X. Huang, B. Li, C. Li *et al.*, "Florence: A new foundation model for computer vision," *arXiv:2111.11432*, 2021. [2](#)
- [33] J. Wang, D. Chen, Z. Wu, C. Luo, L. Zhou, Y. Zhao, Y. Xie, C. Liu, Y.-G. Jiang, and L. Yuan, "Omnivl: One foundation model for image-language and video-language tasks," in *NeurIPS*, 2022. [2](#)
- [34] X. Dong, J. Bao, T. Zhang, D. Chen, W. Zhang, L. Yuan, D. Chen, F. Wen, and N. Yu, "Bootstrapped masked autoencoders for vision bert pretraining," in *ECCV*, 2022, pp. 247–264. [2](#)
- [35] H. Bao, L. Dong, and F. Wei, "Beit: Bert pre-training of image transformers," *ICLR*, 2022. [2](#), [15](#)
- [36] K. He, X. Chen, S. Xie, Y. Li, P. Dollár, and R. Girshick, "Masked autoencoders are scalable vision learners," in *CVPR*, 2022, pp. 16 000–16 009. [2](#), [15](#)
- [37] T. Li, H. Chang, S. Mishra, H. Zhang, D. Katabi, and D. Krishnan, "Mage: Masked generative encoder to unify representation learning and image synthesis," in *CVPR*, 2023, pp. 2142–2152. [2](#), [15](#)
- [38] M. Bertalmio, G. Sapiro, V. Caselles, and C. Ballester, "Image inpainting," in *CGIT*, 2000, pp. 417–424. [2](#)
- [39] A. A. Efros and W. T. Freeman, "Image quilting for texture synthesis and transfer," in *CGIT*, 2001, pp. 341–346. [2](#)
- [40] J. Hays and A. A. Efros, "Scene completion using millions of phoacm trans. graph. raphs," *ACM Trans. Graph.*, vol. 26, no. 3, pp. 4–es, 2007. [2](#)
- [41] R. Suvorov, E. Logacheva, A. Mashikhin, A. Remizova, A. Ashukha, A. Silvestrov, N. Kong, H. Goka, K. Park, and V. Lempitsky, "Resolution-robust large mask inpainting with fourier convolutions," in *WACV*, 2022, pp. 2149–2159. [3](#), [7](#), [8](#), [9](#), [10](#), [12](#)
- [42] G. Liu, A. Dundar, K. J. Shih, T.-C. Wang, F. A. Reda, K. Sapra, Z. Yu, X. Yang, A. Tao, and B. Catanzaro, "Partial convolution for padding, inpainting, and image synthesis," *IEEE Trans. Pattern Anal. Mach. Intell.*, 2022. [3](#)
- [43] C. Zheng, T.-J. Cham, and J. Cai, "Pluralistic image completion," in *CVPR*, 2019, pp. 1438–1447. [3](#), [7](#), [8](#), [12](#)
- [44] L. Zhao, Q. Mo, S. Lin, Z. Wang, Z. Zuo, H. Chen, W. Xing, and D. Lu, "Uctgan: Diverse image inpainting based on unsupervised cross-space translation," in *CVPR*, 2020, pp. 5741–5750. [3](#)
- [45] S. Zhao, J. Cui, Y. Sheng, Y. Dong, X. Liang, E. I. Chang, and Y. Xu, "Large scale image completion via co-modulated generative adversarial networks," in *ICLR*, 2021. [3](#), [7](#), [8](#), [9](#), [10](#), [12](#)
- [46] W. Li, Z. Lin, K. Zhou, L. Qi, Y. Wang, and J. Jia, "Mat: Mask-aware transformer for large hole image inpainting," in *CVPR*, 2022, pp. 10 758–10 768. [3](#), [9](#), [10](#), [12](#)
- [47] T. Karras, S. Laine, M. Aittala, J. Hellsten, J. Lehtinen, and T. Aila, "Analyzing and improving the image quality of stylegan," in *CVPR*, 2020, pp. 8110–8119. [3](#), [9](#), [11](#)
- [48] Q. Liu, Z. Tan, D. Chen, Q. Chu, X. Dai, Y. Chen, M. Liu, L. Yuan, and N. Yu, "Reduce information loss in transformers for pluralistic image inpainting," in *CVPR*, 2022, pp. 11 347–11 357. [4](#), [6](#), [7](#), [8](#), [12](#), [13](#), [14](#)
- [49] E. Jang, S. Gu, and B. Poole, "Categorical reparameterization with gumbel-softmax," *arXiv:1611.01144*, 2016. [4](#), [6](#)
- [50] A. Radford, J. Wu, R. Child, D. Luan, D. Amodei, I. Sutskever *et al.*, "Language models are unsupervised multitask learners," *OpenAI blog*, vol. 1, no. 8, p. 9, 2019. [5](#)
- [51] T.-Y. Lin, M. Maire, S. Belongie, J. Hays, P. Perona, D. Ramanan, P. Dollár, and C. L. Zitnick, "Microsoft coco: Common objects in context," in *ECCV*. Springer, 2014, pp. 740–755. [6](#), [15](#)
- [52] A. Gupta, P. Dollar, and R. Girshick, "Lvis: A dataset for large vocabulary instance segmentation," in *CVPR*, 2019, pp. 5356–5364. [6](#), [15](#)
- [53] A. Lugmayr, M. Danelljan, A. Romero, F. Yu, R. Timofte, and L. Van Gool, "Repaint: Inpainting using denoising diffusion probabilistic models," in *CVPR*, 2022, pp. 11 461–11 471. [7](#), [8](#), [9](#), [12](#)
- [54] D. P. Kingma and J. Ba, "Adam: A method for stochastic optimization," *arXiv:1412.6980*, 2014. [6](#)
- [55] A. Dosovitskiy, L. Beyer, A. Kolesnikov, D. Weissenborn, X. Zhai, T. Unterthiner, M. Dehghani, M. Minderer, G. Heigold, S. Gelly *et al.*, "An image is worth 16x16 words: Transformers for image recognition at scale," *arXiv:2010.11929*, 2020. [6](#), [13](#)
- [56] I. Loshchilov and F. Hutter, "Decoupled weight decay regularization," *arXiv:1711.05101*, 2017. [6](#)
- [57] B. Cheng, I. Misra, A. G. Schwing, A. Kirillov, and R. Girshick, "Masked-attention mask transformer for universal image segmentation," in *CVPR*, 2022, pp. 1290–1299. [6](#), [11](#), [12](#)
- [58] X. Soria, A. Sappa, P. Humanante, and A. Akbarinia, "Dense extreme inception network for edge detection," *Pattern Recognition*, vol. 139, p. 109461, 2023. [6](#)
- [59] H. Liu, B. Jiang, Y. Song, W. Huang, and C. Yang, "Rethinking image inpainting via a mutual encoder-decoder with feature equalizations," in *ECCV*, 2020, pp. 725–741. [7](#), [8](#), [12](#)
- [60] C. Zheng, T.-J. Cham, J. Cai, and D. Phung, "Bridging global context interactions for high-fidelity image completion," in *CVPR*, 2022, pp. 11 512–11 522. [7](#), [8](#), [9](#), [10](#), [12](#)

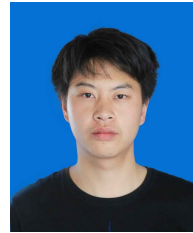
- [61] R. Zhang, P. Isola, A. A. Efros, E. Shechtman, and O. Wang, "The unreasonable effectiveness of deep features as a perceptual metric," in *CVPR*, 2018, pp. 586–595. [8](#), [14](#)
- [62] M. Heusel, H. Ramsauer, T. Unterthiner, B. Nessler, and S. Hochreiter, "Gans trained by a two time-scale update rule converge to a local nash equilibrium," *NeurIPS*, vol. 30, 2017. [8](#)
- [63] Z. Xie, Z. Zhang, Y. Cao, Y. Lin, J. Bao, Z. Yao, Q. Dai, and H. Hu, "Simmin: A simple framework for masked image modeling," in *CVPR*, 2022, pp. 9653–9663. [15](#)
- [64] Y. Li, H. Mao, R. Girshick, and K. He, "Exploring plain vision transformer backbones for object detection," in *ECCV*. Springer, 2022, pp. 280–296. [15](#)



Ying Fu received the B.S. degree in Electronic Engineering from Xidian University in 2009, the M.S. degree in Automation from Tsinghua University in 2012, and the Ph.D. degree in information science and technology from the University of Tokyo in 2015. She is currently a professor with the School of Computer Science and Technology, Beijing Institute of Technology. Her research interests include physics-based vision, image and video processing, and computational photography. She received the Outstanding Paper Award from ICML'20.



Qiankun Liu received his B.S. degree in information engineering from Xidian University in 2017, and Ph.D. degree in information and communication engineering from University of Science and Technology of China in 2022. He is currently a Postdoc. in Beijing Institute of Technology. His research interests detection, person re-identification, object tracking and image synthesis.



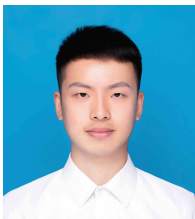
Qi Chu received the B.S. degree in electronic engineering and the Ph.D. degree in information and communication engineering from University of Science and Technology of China in 2014 and 2019, respectively. Currently, he is an associate research fellow at University of Science and Technology of China. His research interests include object detection, tracking, image synthesis and adversarial examples.



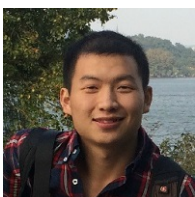
Yuqi Jiang received the Bachelor degree from the School of Computer Science and Technology, Beijing Institute of Technology, Beijing, China, in 2021. He is currently working toward the Master degree with the School of Computer Science, Beijing Institute of Technology. His research interests include image processing, image synthesis, and deep learning.



Gang Hua is the Vice President and Chief Scientist of Wormpex AI Research. Before that, he was the Principal Researcher/Research Manager at Microsoft Research between 2015 to 2018. He was an Associate Professor of Computer Science in Stevens Institute of Technology between 2011 and 2015, while holding an Academic Advisor position at IBM T. J. Watson Research Center. He has published more than 150 peer reviewed papers in top conferences such as CVPR/ICCV/ECCV, and top journals such as T-PAMI and IJCV. To date, he holds 18 issued U.S Patents and also has 14 more U.S. Patents Pending. He is an IEEE Fellow, an IAPR Fellow, and an ACM Distinguished Scientist. His research focuses on artificial intelligence, computer vision, pattern recognition, machine learning, and robotics, with primary applications in the cloud and mobile intelligence domain.



Zhentao Tan received his B.S. and Ph.D. degrees from University of Science and Technology of China in 2017 and 2022, respectively. He is currently a Postdoc. in University of Science and Technology of China. His research interests include semantic segmentation, video object segmentation and image synthesis.



Dongdong Chen is a Principal Researcher from Microsoft Research. He received his Ph.D. degree under the joint phd program between University of Science and Technology of China and MSRA. His research interests mainly include style transfer, image generation, image restoration, low-level image processing, and general representation learning.



Nenghai Yu is a full Professor at University of Science and Technology of China. He is also the director of Information Processing Center of USTC, deputy director of academic committee of School of Information Science and Technology. He received the Ph.D. degree from USTC in 2004. He was a visiting scholar in Institute of Production Technology, Faculty of Engineering, University of Tokyo, in 1999 and did cooperative research as the senior visiting scholar in Dept. of Electrical Engineering, Columbia University, from Apr. to Oct. 2008. His research focuses on image processing and video analysis, multimedia communication, media content security, Internet information retrieval, data mining and content filtering, network communication and security.